Zuse Institute Berlin

Takustr. 7
14195 Berlin
Germany

ADRIAN SALI

Coupling of Monodomain and Eikonal Models for Cardiac Electrophysiology

ZIB Report 16-50 (October 2016)

Zuse Institute Berlin
Takustr. 7
D-14195 Berlin

Telefon: +49 30-84185-0
Telefax: +49 30-84185-125

e-mail: bibliothek@zib.de
URL: http://www.zib.de

ZIB-Report (Print) ISSN 1438-0064
ZIB-Report (Internet) ISSN 2192-7782

Coupling of Monodomain and Eikonal Models for Cardiac Electrophysiology*

Adrian Sali

October 4, 2016

*Thesis submitted for the degree Master of Science in the Department of Mathematics and Computer Science, Free University Berlin. Advisor Dr. Martin Weiser.

Abstract

The primary goal of this paper is to study the coupling of monodomain and eikonal models for the numerical simulation of cardiac electrophysiology.

Eikonal models are nonlinear elliptic equations describing the excitation time of the cardiac tissue. They are often used as very fast approximations for monodomain or bidomain models - parabolic reaction-diffusion systems describing the excitation wavefront in terms of ionic currents. The excitation front is a thin region with high gradients, whereas excitation times vary over larger domains. Hence, eikonal equations can be solved on much coarser grids than monodomain equations. Moreover, as eikonal models are not time-dependent, no time integration is needed.

Eikonal models are derived from monodomain models making additional assumptions and using certain approximations. While generally the approximation is rather good, several specific situations are not well captured by eikonal models. We consider coupling the two models, i.e. using the monodomain model in regions where more accurate results or the shape of the wavefront are needed, and the eikonal model in the remaining parts of the domain, where the excitation time is sufficient. Restricting the monodomain simulation to a small subdomain reduces the computational effort considerably.

Numerical methods for the simulation of the individual models are presented, with the finite element method as the main ingredient. Coupling conditions as well as algorithms for implementing the coupling are explained. The approximation quality and efficiency of the coupled model is illustrated on simple geometries using an Aliev-Panfilov membrane model.

Contents

List of Figures

1 Introduction

Cardiovascular diseases are the leading cause of mortality in the world. In 2012, they led to 17.5 million deaths. This number is expected to increase to 22.2 million by 2030 [33]. In the USA alone, 610'000 people die yearly because of heart diseases, which represents one in four deaths [47]. Thus, the development of improved diagnose and treatment procedures thereof is of utmost importance. This, in turn, requires a better understanding of the actual functioning of the heart.

Current experimental methods of studying the activity of the heart are often too invasive. For example, an electrophysiology study involves the percutaneous introduction of electrode catheters [52]. Unsuitable catheters may lead to punctures in the wall tissue which could lead to internal bleedings [14]. The procedure might also stimulate severe rhythm problems and may, rarely, cause the perforation of the heart [11].

On the other hand, less invasive procedures do not provide the same level of detail. For instance, in electrocardiograms, the solution of an inverse problem is necessary in order to determine the actual activity of the heart. A mathematical model would help determine important physiological parameters by applying realistic physical constraints to the inverse problem [45].

Computational models would not pose risks to the patients. Moreover, they are not subject to the ethics procedures that would be required for performing experiments on either people or animals. Additionally, even when experimental studies are carried out, they never provide measurements for all the functional elements of the heart. Computer simulations would help both in simulating unavailable events and also in understanding better the data acquired.

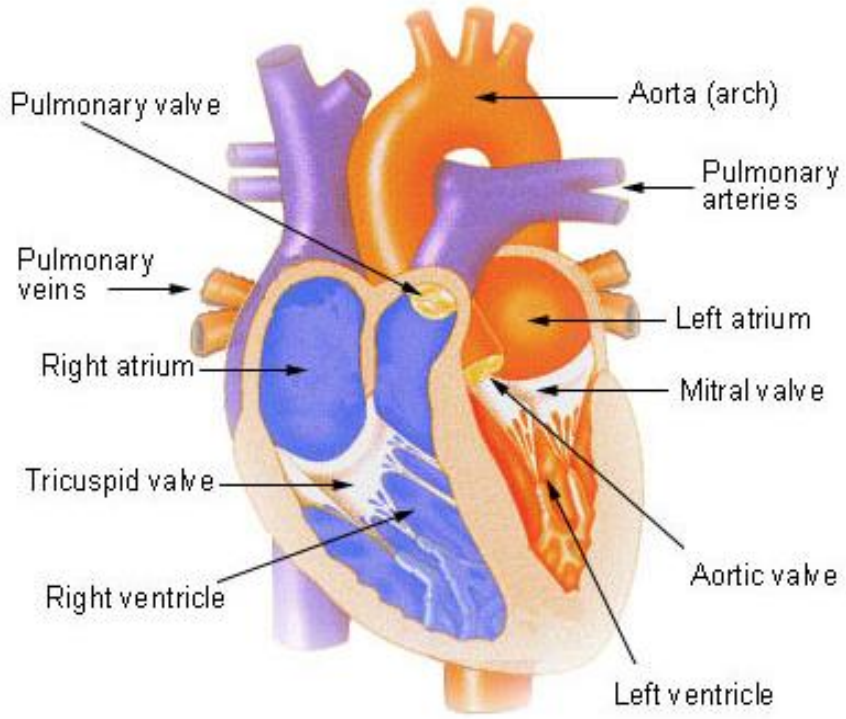

Figure 1.1: Internal view of the heart [42].

1.1 Functioning of the heart

The main role of the heart is pumping blood through the organism. The heart is divided into four chambers: the right atrium and ventricle, and the left atrium and ventricle. Initially, blood enters the right atrium and flows into the right ventricle. It then enters the pulmonary arteries that transport it to the lungs, where it is oxygenated. Through the pulmonary veins it then returns to the left atrium and then flows into the left ventricle. Finally, it is pumped to the body through the aorta. Chambers and blood vessels are separated by valves, which, due to their structure, ensure that the fluid flows in the correct direction.

The actual pumping is realized through the cyclic contraction and relaxation of a muscle structure in the walls of the heart called *myocardium*, which is surrounded by thin layers named *endocardium* - on the inside, and *epicardium* - on the outside. The myocardium consists of discrete cells called *myocytes* that are bounded from

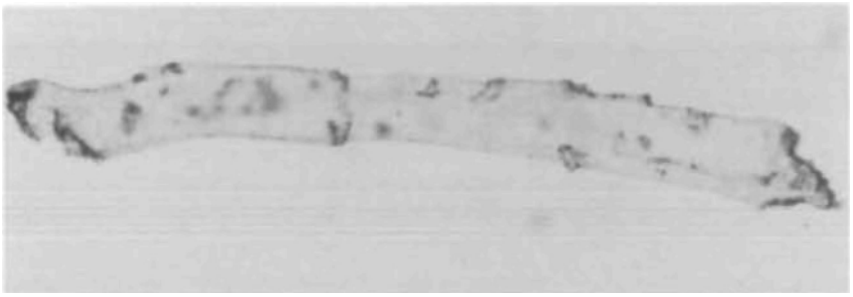

Figure 1.2: Cardiac myocyte [29].

the extracellular space by a membrane - the *sarcolemma*. The myocytes are tube shaped, with a length in between 50 and 120 µm and a diameter in the range between 5 and 25 µm [39]. The extracellular space contains water, electrolytes and collagen fibers among others. For a more detailed discussion on the microscopic structure of the heart, see [39, 44].

The excitation of the heart muscle is caused by an increase in the concentration of intracellular Ca^{2+}, due to its flow from the extracellular space to the interior of the cell, through *ion channels* connecting the two media. Besides Ca^{2+}, there are also Na^+, K^+ and Cl^- ionic currents across the lipid membrane of the cardiac cell. These currents are generated by a wave of electrical activity that propagates through the heart, called *action potential*. The wave is initiated by specialized myocytes in the *sino-atrial node* situated at the top of the right atrium and is made possible by the fact that the cardiac cells are *excitable*, and by the presence of *gap junctions* - proteins that create channels between neighboring cells [43]. Note that due to the tube-like shape of myocytes and their relatively parallel alignment, the myocardial tissue is *anisotropic* and, consequently, the wave does not spread with the same speed in different directions. The speed is higher along the cell and slower in the other directions.

The rise in the concentration of Ca^{2+} is generated by a decrease in the (absolute value of) transmembrane potential difference during *depolarization* (or *upstroke*), the first stage of the action potential. Specifically, during depolarization, the potential difference increases from the resting value of about $-80\,\mathrm{mV}$ to approximately $20\,\mathrm{mV}$. The exact values depend on the area of the heart, age, species and other

physiological factors [5]. Thus, the study of this perturbation (*depolarization wavefront*) is an important step in understanding the functioning of the myocardium. The importance of this is further emphasized by the fact that anomalies in the electrical propagation in the heart lead to or are caused by serious heart problems [43].

1.2 Computational Models

As the sinus node contains more than 100'000 cells, the atrium - several million and the ventricle - hundreds of millions [35], modeling the spread of the electrical excitation by simulating the ionic activity of each cardiac cell is not feasible. Cellular automata have also been used as models of propagation [50], where each cell can be in only a discrete number of states that change at discrete times. Its evolution depends on its state at the previous time step and on its neighboring cells. This model is computationally cheaper, but it has the disadvantage that it's difficult to relate the behavior of cellular automata to electrophysiological observations. Moreover, with a regular lattice, the velocity-curvature relations of the wavefront cannot be simulated readily [22]. Thus, macroscopic models that still observe the electrophysiological aspects are required.

One such model is following the approach now generally known as the *bidomain model* [20], and was initially proposed at the end of the 1970s [46, 23, 10]. The two domains suggested by the model name are represented by the averaged properties of the intracellular and extracellular media. The assumption on these domains is that they are continuous, superposed, they interpenetrate and are connected by a distributed cellular membrane. The current between them depends on the properties of the cell membrane averaged over volume [45, 15]. Furthermore, assuming that the anisotropy ratios of the domains are equal, a *monodomain* model can be derived. In this thesis, the monodomain approach with an ionic model first introduced by Aliev and Panfilov [1] is used. It is represented by a nonlinear reaction-diffusion type system consisting of a parabolic PDE and an ODE. Its solution describes the shape and position of the depolarization wavefront at each moment in time. Further details are explained in Section 2.1. Due to its dependence on both space and time

and, since a fine spatial discretization is needed at the wavefront for accurate results, solving this system is still computationally expensive.

A less accurate *eikonal model*, requiring significantly fewer computing resources, was derived by Keener [25] and Franzoni et al. [15] (see Section 2.2). In contrast to the monodomain approach, the eikonal model does not simulate the shape of the excitation front, but only its position. Specifically, it determines the excitation time for each point in space. However, as it is represented by an elliptic PDE depending only on space variables, no time integration is required for its numerical solution. Moreover, unlike the transmembrane potential, the wave speed usually varies over larger space scales. The gradients of the solution being smaller, a coarser grid can be used for the numerical simulation.

Thus, from an application point of view, it would make sense to use the monodomain model in the areas of the heart where a more accurate and detailed solution is needed, and the eikonal model in the areas where a less accurate solution is sufficient. The goal of this thesis is to present an approach for the coupling of these models.

1.3 Structure of the thesis

In Chapter 2 the monodomain and eikonal models are derived. The former is developed starting from physical laws, like conservation of current and Ohm's Law. The latter is derived from the monodomain model by making additional assumptions and approximations.

Chapter 3 presents numerical solutions for both problems using the finite element method. The linearly implicit Euler method is used for the time discretization of the monodomain equations. The arising linear system is solved using the preconditioned biconjugate gradient stabilized method. The nonlinear system resulting from the discretization of the eikonal equation is solved by an error based damped Newton algorithm.

Consequently, the need for coupling the two models is explained and the coupling conditions and their numerical implementation are described in Chapter 4.

Numerical results are included and discussed in Chapter 5. First, the results corresponding to the individual models are presented and compared. Then, results for the coupling are shown for various geometries and use cases.

Finally, in Chapter 6 the methods and results are summarized and recommendations for further work are suggested.

2 Models of Myocardial Behaviour

2.1 The Monodomain Model

The monodomain model is derived by making some additional assumptions on the bidomain model. Therefore, we will first derive the former and then show its particular case - the monodomain model.

The bidomain model was first introduced by Tung [46] in 1978. It approximates the intracellular and extracellular media as continuous spaces, that co-exist spatially and that are separated by a cell membrane which is continuous as well and that fills the entire volume. The spatial co-existence means that each point is part of both media. The intracellular space can be considered continuous due to the gap junctions between cells, which allow direct interaction between their internals. The cell membrane has the role of insulating the two domains, which creates the potential differences mentioned in the introductory chapter. Nonetheless, channels passing through it allow ions to move from one medium to the other, thus creating a current that depends on the potential difference between the two domains (*transmembrane potential*) and on the permeability of the membrane. Due to continuity of the domains, at each point we have a potential, that, from a physical point of view, is the average over a small surrounding volume.

2.1.1 Derivation of the model

Let J_i and J_e be the intracellular and extracellular current densities respectively. Assuming they each obey Ohm's Law, we have

$$J_i = -M_i \nabla u_i, \tag{2.1}$$

$$J_e = -M_e \nabla u_e, \tag{2.2}$$

where u_i and u_j are the potentials of the domains, whereas M_i and M_e are the conductivities of the media. As heart tissue is anisotropic, these are tensor quantities. Moreover, if we assume that capacitive, inductive, and electromagnetic propagative effects can be neglected, conservation of current gives

$$\nabla \cdot J_i = -i_m, \tag{2.3}$$

$$\nabla \cdot J_e = i_m + i_{app}, \tag{2.4}$$

where i_m is the outward transmembrane current per unit volume, and i_{app} is an applied current per unit tissue volume.

Summing up (2.3) and (2.4) results in

$$\nabla \cdot J_i + \nabla \cdot J_e = i_{app}, \tag{2.5}$$

and plugging in (2.1) and (2.2) into (2.5), we obtain

$$\nabla \cdot (M_i \nabla u_i) + \nabla \cdot (M_e \nabla u_e) = -i_{app}. \tag{2.6}$$

Now let $v := u_i - u_e$ be the transmembrane potential. The net current through the membrane is equal to the sum of the ionic and capacitive components:

$$i_m = \chi I_{ion} + \chi C_m \frac{\partial v}{\partial t}. \tag{2.7}$$

Here, C_m is the capacitance of the membrane measured per unit area. The voltage/current relationship for capacitance $I(t) = C\frac{\partial V(t)}{\partial t}$ has been used for the capacitive component. Additionally, a constant χ representing the area of cell membrane per unit volume is introduced. The current I_{ion} is also measured per unit area.

Combining (2.1), (2.3) and (2.7), we obtain

$$\nabla \cdot (M_i \nabla u_i) = \chi I_{ion} + \chi C_m \frac{\partial v}{\partial t}, \tag{2.8}$$

and using $u_i = v + u_e$ in (2.8) and (2.6) we get the following system

$$\nabla \cdot (M_i \nabla (v + u_e)) = \chi I_{ion} + \chi C_m \frac{\partial v}{\partial t}, \tag{2.9}$$

$$\nabla \cdot (M_i \nabla (v + u_e)) + \nabla \cdot (M_e \nabla u_e) = -i_{app}. \tag{2.10}$$

Finally, a rearrangement of terms results in the bidomain model

$$\nabla \cdot (M_i \nabla v) + \nabla \cdot (M_i \nabla u_e) = \chi I_{ion} + \chi C_m \frac{\partial v}{\partial t}, \tag{2.11}$$

$$\nabla \cdot (M_i \nabla v) + \nabla \cdot ((M_i + M_e) \nabla u_e) = -i_{app}. \tag{2.12}$$

For a full description of the model, boundary conditions are needed. In addition to conservation of current between the intracellular and extracellular domain, this condition should also be fulfilled between the heart muscle and the outside volume:

$$n \cdot (J_i + J_e) = n \cdot J_o, \tag{2.13}$$

where n is the boundary unit normal, while J_o is the current density corresponding to the outside volume. Moreover, assuming that only the extracellular space is in contact with the outside volume, it was shown [27] that the boundary condition

$$n \cdot J_i = 0 \tag{2.14}$$

should be satisfied. Using (2.1) and substituting u_i by $v + u_e$, this last relation is equivalent to

$$n \cdot M_i \nabla (v + u_e) = 0, \tag{2.15}$$

whereas (2.13) becomes

$$n \cdot M_e \nabla u_e = n \cdot M_o \nabla u_o, \tag{2.16}$$

where u_o is the potential of the outside volume, and M_o is the respective conductivity tensor. We should also mention, that since the extracellular domain is in direct

contact with the outer medium, the condition $u_e = u_o$ should be satisfied.

In this thesis, we assume that the medium surrounding the heart is non-conductive. Thus, in summary, the bidomain model can be formulated as follows:

$$\nabla \cdot (M_i \nabla v) + \nabla \cdot (M_i \nabla u_e) = \chi I_{ion} + \chi C_m \frac{\partial v}{\partial t} \qquad \text{on } \Omega, \tag{2.17}$$

$$\nabla \cdot (M_i \nabla v) + \nabla \cdot ((M_i + M_e) \nabla u_e) = -i_{app} \qquad \text{on } \Omega, \tag{2.18}$$

$$v(0, \boldsymbol{x}) = v_0(\boldsymbol{x}) \qquad \text{on } \Omega, \tag{2.19}$$

$$u_e(0, \boldsymbol{x}) = u_{e_0}(\boldsymbol{x}) \qquad \text{on } \Omega, \tag{2.20}$$

$$n \cdot M_i \nabla (v + u_e) = 0 \qquad \text{on } \partial\Omega, \tag{2.21}$$

$$n \cdot M_e \nabla u_e = 0 \qquad \text{on } \partial\Omega. \tag{2.22}$$

For the derivation of the monodomain model, the assumption of *equal anisotropy ratios* is made, i.e. $M_e = \lambda M_i$, for some constant scalar λ. Substituting this into (2.18) gives

$$\nabla \cdot (M_i \nabla v) + (1 + \lambda) \nabla \cdot (M_i \nabla u_e) = -i_{app}, \tag{2.23}$$

equivalent to

$$\nabla \cdot (M_i \nabla u_e) = -\frac{1}{1+\lambda} i_{app} - \frac{1}{1+\lambda} \nabla \cdot (M_i \nabla v). \tag{2.24}$$

Replacing this in (2.17), we obtain

$$\frac{\lambda}{1+\lambda} \nabla \cdot (M_i \nabla v) - \frac{1}{1+\lambda} i_{app} = \chi I_{ion} + \chi C_m \frac{\partial v}{\partial t}. \tag{2.25}$$

Equation (2.22) becomes

$$n \cdot (\lambda M_i \nabla u_e) = 0, \tag{2.26}$$

and inserting this into (2.21), we get

$$n \cdot (M_i \nabla v) = 0. \tag{2.27}$$

Now, for v_r - the resting potential, let

$$\frac{1}{R_m} := \frac{dI_{ion}}{dv}(v_r) \qquad \text{and} \qquad \frac{1}{r_m} := \chi \frac{1}{R_m}, \tag{2.28}$$

and $\overline{r}_m$ be the space average of r_m. Further, define

$$\tau_m := \overline{r}_m \chi C_m, \qquad M_m := \overline{r}_m \frac{\lambda}{1+\lambda} M_i, \qquad \text{and} \qquad f_{ion} := \overline{r}_m \chi I_{ion}. \tag{2.29}$$

Again, rearranging and summarizing, we have the following monodomain model:

$$\tau_m \frac{\partial v}{\partial t} = \nabla \cdot (M_m \nabla v) - \overline{r}_m \frac{1}{1+\lambda} i_{app} - f_{ion} \qquad \text{on } \Omega \tag{2.30}$$

$$n \cdot (M_m \nabla v) = 0 \qquad \text{on } \partial\Omega. \tag{2.31}$$

Nondimensionalizing quantities, we obtain the form:

$$\frac{\partial V}{\partial \tau} = \nabla \cdot (M \nabla V) + I_{app} - F_{ion} \qquad \text{on } \Omega \tag{2.32}$$

$$n \cdot (M \nabla V) = 0 \qquad \text{on } \partial\Omega. \tag{2.33}$$

2.1.2 Ionic Models

Finally, in order to solve these equations, a model for the ionic current I_{ion} (F_{ion} respectively) is necessary. Currently, three main groups of ionic models are used [43].

The models in the first one, called first generation, depict the ionic currents that have the biggest role for the action potential, and describe both the cellular behavior and the underlying physiology. Such models, however, do not describe fine-scale physiological details. Hodgkin and Huxley first proposed a model of this kind [21]. It included a sodium, a potassium and a third current called leakage current. The main disadvantage of this model in our case, however, is that it describes the action potential in a squid giant axon, and is, therefore, not directly applicable to myocardial cells. Later, in 1962, Noble [34] adapted it to work with the Purkinje fibre cells, a tree-like structure located in the subendocardium. The leakage current is assumed to be zero in this case, and the potassium current is separated into two distinct ones. However, detailed physiological data had not yet been determined experimentally at that time. Thus, the physiology behind the model was not accurate. It was enhanced by improving the accuracy of the previously used ionic channels and by adding new

ones in 1975 [32]. A model specific to ventricular cells was first introduced by Beeler and Reuter [3] around the same time. Here, two outward potassium, one inward calcium and one inward sodium currents are considered. Thus, it also depicts the intracellular concentration of calcium, which has the main role in muscle contraction. One final first generation model that we will mention here is due to Luo and Rudy [31]. In addition to the Beeler-Reuter model, it decribes an additional potassium current and a linear background current, comparable to the leakage current used by Hodgkin and Huxley. Both these models are still widely used today.

Luo and Rudy significantly improved their model in 1994 [30]. Describing twelve currents - including intracellular sodium, potassium and three distinct calcium concentrations - and several internal fluxes, this concept is part of the next group, called second generation models. Other models that handle calcium ions differently have been introduced in 1998 by Noble er al. [36] and by Jafri et al. [24]. In 1999, Winslow et al. [51] proposed a similar model adapted to data from dogs. It includes more than 30 state variables that control 13 ionic currents. It was later improved to a model that contains several thousand variables by Greenstein and Winslow [19], and was simplified by Greenstein et al. in 2006 [18]. Approaches using fractional differential equations have also been suggested recently [49].

In the third group, phenomenological models are included. They simulate the ionic current macroscopically, not at a cellular level. These are usually FitzHugh-Nagumo [13] type models, with two variables. The first one is the transmembrane potential, whereas the second one represents a gating variable. Thus, they are computationally much cheaper, but they still reproduce the main characteristics of cardiac tissue. Modifications of the simplified FitzHugh-Nagumo equations have been introduced in 1991 by Kogan et al. [26], and by Rogers and McCulloch in 1994 [37]. The latter has been further improved by Aliev and Panfilov in 1996 [1] by introducing a nonlinearity in the description of the gating variable. Further, a model with two gating variables was proposed by Fenton and Karma in 1998 [12].

Since our main goal is to study the propagation of the depolarization wavefront, which is affected primarily by macroscopic properties, a model pertaining to the third category described is used in this thesis, specifically, the Aliev-Panfilov approach.

In this case, the monodomain model becomes:

$$\frac{\partial V}{\partial \tau} = \nabla \cdot (M \nabla V) \underbrace{-g_a V(V-a)(V-1) - Vw + I_{app}}_{:=f(V,w)} \qquad \text{in } \Omega \times (0,T), \tag{2.34}$$

$$\frac{\partial w}{\partial \tau} = \underbrace{\left(\epsilon_1 + \mu_1 \frac{w}{V+\mu_2}\right)(-w - g_s V(V-b-1))}_{:=g(V,w)} \qquad \text{in } \Omega \times (0,T), \tag{2.35}$$

$$V(0,\boldsymbol{x}) = V_0(\boldsymbol{x}) \qquad \text{in } \Omega, \tag{2.36}$$

$$w(0,\boldsymbol{x}) = w_0(\boldsymbol{x}) \qquad \text{in } \Omega, \tag{2.37}$$

$$n \cdot (M \nabla V) = 0 \qquad \text{on } \partial\Omega \times (0,T), \tag{2.38}$$

$$n \cdot (M \nabla w) = 0 \qquad \text{on } \partial\Omega \times (0,T). \tag{2.39}$$

Here all the terms are non-dimensional, the derivatives included. V is a representation of the potential difference across the membrane and varies between 0 (polarized state) and 1 (depolarized state), w is a gating variable that corresponds to the conduction of a repolarising current, I_{app} is the applied current and a is a threshold parameter. The capacitance is included implicitly. Parameters g_a, ϵ_1, μ_1, μ_2, g_s, and b have no physiological meaning. Assuming a resting potential value of $-80\,\text{mV}$ and an action potential amplitude of $100\,\text{mV}$, the real physical value of the transmembrane potential can be determined using

$$E\ [mV] = 100V - 80. \tag{2.40}$$

Existence of solutions for the weak formulation of a similar model, where the first factor in $g(V,w)$ is assumed to be a constant, was shown in [4].

2.2 The Eikonal Model

In many cases only the motion of the depolarization wavefront is of interest, and not its shape. Under the assumption that the depolarization process starts only in tissue at rest, a simplified model, called the *eikonal model*, can be derived. For each point $\boldsymbol{x}$ in space, it determines its excitation time $u(\boldsymbol{x})$, i.e. the time when the transmembrane potential at the respective point is at the middle value between the

resting and plateau potentials. The model was derived using singular perturbation techniques by Franzoni, Guerri, and Rovida [15]. In this chapter, we will, however, summarize the approach used by Tomlinson [45].

According to the definition of $u(\boldsymbol{x})$ above, we have

$$v(\boldsymbol{x}, u(\boldsymbol{x})) = \frac{1}{2}(v_r + v_p), \tag{2.41}$$

where v_r and v_p are the resting and plateau transmembrane potentials.

In a healthy heart, the shape of the upstroke does not change significantly along the tissue. Therefore, we may write

$$v(\boldsymbol{x}, t) = v_m(\omega), \tag{2.42}$$

where $v_m : \mathbb{R} \to \mathbb{R}$ is some function of variable ω, which is defined such that

$$v(\boldsymbol{x}, u(\boldsymbol{x})) = v_m(\omega = 0). \tag{2.43}$$

The change in coordinates

$$\boldsymbol{x} = \boldsymbol{\xi} \text{ and } t = T(\boldsymbol{\xi}, \omega), \tag{2.44}$$

therefore implies that

$$u(\boldsymbol{x}) = T(\boldsymbol{\xi}, 0). \tag{2.45}$$

Define $S(\boldsymbol{\xi}, \omega)$ by

$$S := \left(\frac{\partial T}{\partial \omega}\right)^{-1}. \tag{2.46}$$

The chain rule gives

$$\frac{\partial}{\partial \omega} = \sum_{j=1}^{d} \frac{\partial x_j}{\partial \omega}\frac{\partial}{\partial x_j} + \frac{\partial t}{\partial \omega}\frac{\partial}{\partial t} = \frac{\partial T}{\partial \omega}\frac{\partial}{\partial t},$$

or

$$\frac{\partial}{\partial t} = S\frac{\partial}{\partial \omega}. \tag{2.47}$$

Similarly,

$$\frac{\partial}{\partial \xi_i} = \sum_{j=1}^{d} \frac{\partial x_j}{\partial \xi_i}\frac{\partial}{\partial x_j} + \frac{\partial t}{\partial \xi_i}\frac{\partial}{\partial t} = \frac{\partial}{\partial x_i} + \frac{\partial T}{\partial \xi_i}\frac{\partial}{\partial t} = \frac{\partial}{\partial x_i} + \frac{\partial T}{\partial \xi_i} S \frac{\partial}{\partial \omega},$$

or

$$\frac{\partial}{\partial x_i} = \frac{\partial}{\partial \xi_i} - \frac{\partial T}{\partial \xi_i} S \frac{\partial}{\partial \omega}. \tag{2.48}$$

Let us rewrite (2.30) in the original coordinates and using partial derivatives, assuming no external current is applied. We obtain

$$\tau_m \frac{\partial v}{\partial t} = \sum_{i=1}^{d} \frac{\partial}{\partial x_i}\left(\sum_{j=1}^{d} \mu_{ij}\frac{\partial v}{\partial x_j}\right) - f_{ion}, \tag{2.49}$$

where μ_{ij} are the elements of tensor M_m. Remembering that v_m is only a function of ω in the coordinates, we have

$$\frac{\partial v}{\partial x_j} = \left(\frac{\partial}{\partial \xi_j} - \frac{\partial T}{\partial \xi_j} S \frac{\partial}{\partial \omega}\right) v_m = -\frac{\partial T}{\partial \xi_j} S \frac{\partial v_m}{\partial \omega}. \tag{2.50}$$

Further, as M_m is independent of ω, we obtain

$$\begin{aligned}
\frac{\partial}{\partial x_i}\left(\mu_{ij}\frac{\partial v}{\partial x_j}\right) &= \left(\frac{\partial}{\partial \xi_i} - \frac{\partial T}{\partial \xi_i} S \frac{\partial}{\partial \omega}\right)\left(-\mu_{ij}\frac{\partial T}{\partial \xi_j} S \frac{\partial v_m}{\partial \omega}\right) \\
&= -\frac{\partial}{\partial \xi_i}\left(\mu_{ij} S \frac{\partial T}{\partial \xi_i}\right)\frac{\partial v_m}{\partial \omega} + \frac{\partial T}{\partial \xi_i} S \mu_{ij} \frac{\partial}{\partial \omega}\left(S \frac{\partial T}{\partial \xi_j}\frac{\partial v_m}{\partial \omega}\right) \\
&= -\frac{\partial}{\partial \xi_i}\left(\mu_{ij} S \frac{\partial T}{\partial \xi_i}\right)\frac{\partial v_m}{\partial \omega} \\
&\quad + \frac{\partial T}{\partial \xi_i} S \mu_{ij}\left(\frac{\partial}{\partial \omega}\left(S \frac{\partial T}{\partial x_j}\right)\frac{\partial v_m}{\partial \omega} + S \frac{\partial T}{\partial x_j}\frac{\partial^2 v_m}{\partial \omega^2}\right) \\
&= -\frac{\partial}{\partial \xi_i}\left(\mu_{ij} S \frac{\partial T}{\partial \xi_i}\right)\frac{\partial v_m}{\partial \omega} \\
&\quad + S \frac{\partial T}{\partial \xi_i}\frac{\partial}{\partial \omega}\left(\mu_{ij} S \frac{\partial T}{\partial \xi_j}\right)\frac{\partial v_m}{\partial \omega} + S^2 \frac{\partial T}{\partial \xi_i}\mu_{ij}\frac{\partial T}{\partial \xi_j}\frac{\partial^2 v_m}{\partial \omega^2}
\end{aligned} \tag{2.51}$$

Thus, using the Einstein notation for summation, equation (2.30) becomes:

$$\left(\tau_m S + \frac{\partial}{\partial \xi_i}\left(S\mu_{ij}\frac{\partial T}{\partial \xi_j}\right) - \frac{1}{2}\frac{\partial}{\partial \omega}\left(S^2\frac{\partial T}{\partial \xi_i}\mu_{ij}\frac{\partial T}{\partial \xi_j}\right)\right)\frac{dv_m}{d\omega} = S^2\frac{\partial T}{\partial \xi_i}\mu_{ij}\frac{\partial T}{\partial \xi_j}\frac{d^2 v_m}{d\omega^2} - f_{ion}. \tag{2.52}$$

We will now be looking for a first order approximation

$$T(\boldsymbol{\xi}, \omega) := T(\boldsymbol{\xi}, 0) + \frac{\omega}{S(\boldsymbol{\xi}, 0)} = u(\boldsymbol{\xi}) + \frac{\omega}{s(\boldsymbol{\xi})}, \tag{2.53}$$

that fits (2.52) as well as possible, where $s(\boldsymbol{\xi}) := S(\boldsymbol{\xi}, 0)$. Therefore, we want to minimize the residual

$$f_{ion} + \left(\tau_m s + \frac{\partial}{\partial \xi_i}\left(s\mu_{ij}\frac{\partial T}{\partial \xi_j}\right) - \frac{1}{2}\frac{\partial}{\partial \omega}\left(s^2\frac{\partial T}{\partial \xi_i}\mu_{ij}\frac{\partial T}{\partial \xi_j}\right)\right)\frac{dv_m}{d\omega} - s^2\frac{\partial T}{\partial \xi_i}\mu_{ij}\frac{\partial T}{\partial \xi_j}\frac{d^2 v_m}{d\omega^2}. \tag{2.54}$$

Simplifying, (2.54) becomes

$$f_{ion} + \left(\tau_m s + s\frac{\partial}{\partial \xi_i}\left(\mu_{ij}\frac{\partial T}{\partial \xi_j}\right)\right)\frac{dv_m}{d\omega} - \frac{\partial}{\partial \omega}\left(s^2\frac{\partial T}{\partial \xi_i}\mu_{ij}\frac{\partial T}{\partial \xi_j}\frac{dv_m}{d\omega}\right) \tag{2.55}$$

To minimize this residual for all ω, two (since two parameters – u and s – need to be determined) weighted integrals are set to zero. As we move away from the wavefront, the propagation is less and less affected by the features at that point. Therefore, Gaussians are selected as weights, specifically:

$$w_1 = e^{-\alpha\omega^2} \qquad \text{and} \qquad w_2 = \omega e^{-\alpha\omega^2}. \tag{2.56}$$

Thus, we need

$$\int_{-\infty}^{\infty} f_{ion} w_1 d\omega + \int_{-\infty}^{\infty}\left(\tau_m s + s\frac{\partial}{\partial \xi_i}\left(\mu_{ij}\frac{\partial T}{\partial \xi_j}\right)\right)\frac{dv}{d\omega} w_1 d\omega = \int_{-\infty}^{\infty}\frac{\partial}{\partial \omega}\left(s^2\frac{\partial T}{\partial \xi_i}\mu_{ij}\frac{\partial T}{\partial \xi_j}\frac{dv}{d\omega}\right) w_1 d\omega. \tag{2.57}$$

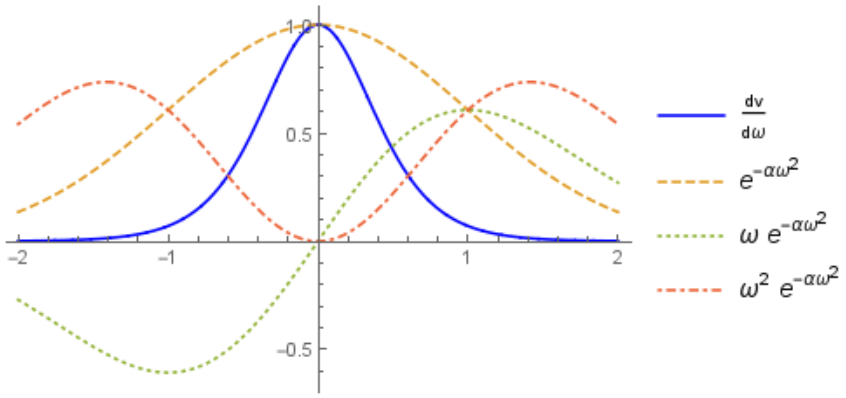

Figure 2.1: Comparison of the terms inside the integrals in (2.58).

Applying Green's theorem, and using (2.53) and (2.56), this becomes:

$$\begin{aligned}
\int_{-\infty}^{\infty} f_{ion} e^{-\alpha\omega^2} d\omega + \left(\tau_m s + s\frac{\partial}{\partial \xi_i}\left(\mu_{ij}\frac{\partial u}{\partial \xi_j}\right)\right) \int_{-\infty}^{\infty} \frac{dv_m}{d\omega} e^{-\alpha\omega^2} d\omega \\
+ s\frac{\partial}{\partial \xi_i}\left(\mu_{ij}\frac{\partial}{\partial \xi_j}\left(\frac{1}{s}\right)\right) \int_{-\infty}^{\infty} \frac{dv_m}{d\omega} \omega e^{-\alpha\omega^2} d\omega \\
= 2\alpha s^2 \frac{\partial u}{\partial \xi_j}\mu_{ij}\frac{\partial u}{\partial \xi_j} \int_{-\infty}^{\infty} \frac{dv_m}{d\omega} \omega e^{-\alpha\omega^2} d\omega \\
+ 4\alpha s^2 \frac{\partial}{\partial \xi_i}\left(\frac{1}{s}\right)\mu_{ij}\frac{\partial u}{\partial \xi_j} \int_{-\infty}^{\infty} \frac{dv_m}{d\omega} \omega^2 e^{-\alpha\omega^2} d\omega \\
+ 2\alpha s^2 \frac{\partial}{\partial \xi_i}\left(\frac{1}{s}\right)\mu_{ij}\frac{\partial}{\partial \xi_j}\left(\frac{1}{s}\right) \int_{-\infty}^{\infty} \frac{dv_m}{d\omega} \omega^3 e^{-\alpha\omega^2} d\omega. \quad (2.58)
\end{aligned}$$

Here, all integrals are constant. Further, it can be shown by dimensional analysis (see [45] for details) that, by picking the scale of ω such that most of the variation in v occurs over a unit change in ω, all terms on the right of the equation are small compared to the second term on the left hand side. The same holds for the last term on the left. The motivation for that can be seen in Fig. 2.1, where the derivative of the expected front shape is plotted together with $e^{-\alpha\omega^2}$, $\omega e^{-\alpha\omega^2}$, and $\omega^2 e^{-\alpha\omega^2}$

for $\alpha = 0.5$. One notices that the addition of ω in the products results in the fact that the respective terms are small in the interval where the derivative of the potential is large and vice-versa. Removing the insignificant terms, only the first two components of the equation are left and we have the following approximation:

$$\tau_m s + s\frac{\partial}{\partial \xi_i}\left(\mu_{ij}\frac{\partial u}{\partial \xi_j}\right) \approx c_2, \tag{2.59}$$

for some constant c_2.

Using the second weight parameter in (2.56), a similar reasoning leads to the second equation for u and s:

$$s^2\frac{\partial u}{\partial \xi_i}\mu_{ij}\frac{\partial u}{\partial \xi_j} \approx c_1^2. \tag{2.60}$$

Using the same coordinate transformation in (2.31), we get that

$$\frac{\partial T}{\partial \xi_i}\mu_{ij}n_j = 0, \tag{2.61}$$

which at $\omega = 0$ becomes

$$\frac{\partial u}{\partial \xi_i}\mu_{ij}n_j = 0 \qquad \text{on } \partial\Omega. \tag{2.62}$$

Returning to the original coordinate system and summarizing (2.59), (2.60), and (2.62), we obtain the system:

$$s\sqrt{\frac{\partial u}{\partial x_i}\mu_{ij}\frac{\partial u}{\partial x_j}} = c_1 \qquad \text{on } \Omega, \tag{2.63}$$

$$\tau_m s + s\frac{\partial}{\partial x_i}\left(\mu_{ij}\frac{\partial u}{\partial x_j}\right) = c_2 \qquad \text{on } \Omega, \tag{2.64}$$

$$\frac{\partial u}{\partial x_i}\mu_{ij}n_j = 0 \qquad \text{on } \partial\Omega. \tag{2.65}$$

Eliminating the variable s from this system finally gives the *eikonal model*

$$c_0\sqrt{\nabla u \cdot M_m \nabla u} - \nabla \cdot (M_m \nabla u) = \tau_m \qquad \text{on } \Omega, \tag{2.66}$$

$$\boldsymbol{n} \cdot M\nabla u + \alpha u = \beta \qquad \text{on } \partial\Omega, \tag{2.67}$$

Symbol	Name	Unit	SI unit
J	Current density	$\mathrm{A} \cdot \mathrm{m}^{-2}$	$\mathrm{A} \cdot \mathrm{m}^{-2}$
u, v	Potential	V	V
M	Conductivity	$\Omega^{-1} \cdot \mathrm{m}^{-1}$	$\mathrm{kg}^{-1} \cdot \mathrm{m}^{-3} \cdot \mathrm{s}^{3} \cdot \mathrm{A}^{2}$
i	Current (per unit volume)	$\mathrm{A} \cdot \mathrm{m}^{-3}$	$\mathrm{A} \cdot \mathrm{m}^{-3}$
I_{ion}	Ionic current (per unit area)	$\mathrm{A} \cdot \mathrm{m}^{-2}$	$\mathrm{A} \cdot \mathrm{m}^{-2}$
C	Capacitance (per unit area)	$\mathrm{F} \cdot \mathrm{m}^{-2}$	$\mathrm{s}^{4} \cdot \mathrm{A}^{2} \cdot \mathrm{m}^{-4} \cdot \mathrm{kg}^{-1}$
χ	-	m^{-1}	m^{-1}
M_m	Coupling tensor	m^{2}	m^{2}
τ_m	Membrane time constant	s	s

Table 2.1: Units of the important parameters and variables.

where $c_0 := \frac{c_2}{c_1}$. As we assumed no external current applied, to "initiate" the front, Dirichlet boundary conditions have to be assigned on some regions of the boundary. Therefore, the boundary conditions have been generalized to Robin type.

To conclude the chapter, Table 2.1 contains a summary of the most important parameters and variables used in the model with their corresponding units physical.

3 Numerical Solution Methods

The monodomain and eikonal systems can only be solved analytically for a small set of particular cases. For example, the exact solution of the eikonal model can be determined in the case of an infinite homogeneous domain, where it describes an ellipsoidal wavefront. For physically relevant domains, however, analytic solutions cannot be determined. Therefore, numerical methods are employed to obtain approximate solutions. In this chapter we will present such methods for 2D domains. The main ingredient here is the finite element method (FEM). For an in depth discussion of the foundations of this method, see, for example, [2].

3.1 The Monodomain Model

The monodomain model is represented by a time- and space-dependent system of equations. A discretization in both dimensions is therefore needed. The time integration is done using the linearly implicit Euler method, whereas space discretization is implemented using the finite element method.

3.1.1 Time discretization

The monodomain model (2.34) - (2.39) is of the form

$$\dot{y} = F(y), \tag{3.1}$$

where

$$y = \begin{pmatrix} V \\ w \end{pmatrix}, \tag{3.2}$$

and F is a functional representing the right hand side.

The time domain $[0, T]$ is divided into subintervals $0 = t_0 < \cdots < t_f < T$. Then, the system is solved using the linearly implicit Euler method. Specifically, we have the discretization

$$\frac{y_{k+1} - y_k}{t_{k+1} - t_k} = F(y_{k+1}). \tag{3.3}$$

Next, we linearize the right hand side to obtain

$$\frac{\delta y_k}{\delta t_k} = F(y_k) + (F_y(y_k))\delta y_k, \tag{3.4}$$

where we denoted $\delta y_k := y_{k+1} - y_k$ and $\delta t_k := t_{k+1} - t_k$. A rearrangement then gives

$$(I - \delta t_k F_y(y_k))\delta y_k = \delta t_k F(y_k), \tag{3.5}$$

where I is the identity operator.

The solution at the new time step can then obviously be determined using

$$y_{k+1} = y_k + \delta y_k. \tag{3.6}$$

The order of accuracy of the scheme could be improved by combining this approach with τ-extrapolation, resulting in the so called extrapolated linearly implicit Euler method [6]. For implementation details see [8].

Applying (3.5) to the monodomain equations gives

$$\begin{aligned} -\delta t_k \left(\nabla \cdot M \nabla \delta V_k\right) + (1 - \delta t_k f_V(V_k, w_k))\delta V_k \\ -\delta t_k f_w(V_k, w_k)\delta w_k = \delta t_k \nabla \cdot M \nabla V_k + \delta t_k f(V_k, w_k), \end{aligned} \tag{3.7}$$

$$-\delta t_k g_V(V_k, w_k)\delta V_k + (1 - \delta t_k g_w(V_k, w_k))\delta w_k = \delta t_k g(V_k, w_k), \tag{3.8}$$

where

$$f_V(V_k, w_k) = -g_a\left((2V_k - a)(V_k - 1) + V_k(V_k - a)\right) - w_k, \tag{3.9}$$

$$f_w(V_k, w_k) = -V_k, \tag{3.10}$$

$$\begin{aligned} g_V(V_k, w_k) = \mu_1 \frac{w_k}{(V_k + \mu_2)^2}(-w_k - g_s V_k(V_k - b - 1)) \\ + \left(\epsilon_1 + \mu_1 \frac{w_k}{V + \mu_2}\right)(-g_s(2V_k + b + 1)), \end{aligned} \tag{3.11}$$

$$g_w(V_k, w_k) = \frac{\mu_1}{V_k + \mu_2}(-w_k - g_s V_k(V_k - b - 1)) - \left(\epsilon_1 + \mu_1 \frac{w_k}{V_k + \mu_2}\right). \tag{3.12}$$

3.1.2 Space discretization

Notice the presence in (3.7) of the elliptic operator $\nabla \cdot M\nabla$ acting on δV_k. Therefore, at each time step we need to solve a stationary linear elliptic problem. To do that, we rewrite the system in its weak form, by multiplying each equation with a test function, integrating over the space domain and applying Green's first identity. We obtain:

$$\begin{aligned} \delta t_k \int_\Omega \nabla \delta V_k \cdot M\nabla\phi dx - \delta t_k \int_{\partial\Omega} \boldsymbol{n} \cdot M\nabla\delta V_k \phi dx + \int_\Omega (1 - \delta t_k f_V(V_k, w_k))\delta V_k \phi dx \\ -\delta t_k \int_\Omega f_w(V_k, w_k)\delta w_k \phi dx = \delta t_k \int_\Omega (\nabla \cdot M\nabla V_k + f(V_k, w_k))\phi dx \\ \forall \phi \in H^1(\Omega), \end{aligned} \tag{3.13}$$

$$\begin{aligned} -\delta t_k \int_\Omega g_V(V_k, w_k)\delta V_k \psi dx + \int_\Omega (1 - \delta t_k g_w(V_k, w_k))\delta w_k \psi dx = \delta t_k \int_\Omega g(V_k, w_k)\psi dx \\ \forall \psi \in L^2(\Omega). \end{aligned} \tag{3.14}$$

Note that the model we are using assumes homogeneous Neumann boundary conditions, so, in theory the integral over the boundary of the domain should vanish in equation (3.13). However, due to reasons displayed in Sec. 4.3, this assumption does not hold on all the boundaries when coupling the model. Therefore, we generalize

the boundary conditions to Robin type, i.e.

$$\boldsymbol{n} \cdot M\nabla\delta V_k + \alpha\delta V_k = \beta \qquad \text{on } \delta\Omega. \tag{3.15}$$

Plugging this into equation (3.13), it becomes

$$\begin{aligned} &\delta t_k \int_\Omega \nabla\delta V_k \cdot M\nabla\phi dx + \delta t_k \int_{\partial\Omega} \alpha\delta V_k\phi dx + \int_\Omega (1 - \delta t_k f_V(V_k, w_k))\delta V_k\phi dx \\ -\delta t_k &\int_\Omega f_w(V_k, w_k)\delta w_k\phi dx = \delta t_k \int_{\partial\Omega} \beta\phi dx + \delta t_k \int_\Omega (\nabla \cdot M\nabla V_k + f(V_k, w_k))\phi dx \\ &\qquad\qquad\qquad\qquad\qquad\qquad\qquad\qquad\qquad\qquad \forall\phi \in H^1(\Omega), \end{aligned} \tag{3.16}$$

In the regions of the boundary where we have a homogeneous Neumann boundary condition, α and β are set to 0. On the Dirichlet boundary, however, we pick a very large α ($\approx 10^8$), and let $\beta := \alpha\delta V_{k_0}$, to introduce a penalty for the Neumann part of the equation. Here, δV_{k_0} represents the known value of the solution on the Dirichlet boundary.

Solving this problem in the infinitely dimensional space $H^1(\Omega) \times L^2(\Omega)$ is not possible. Therefore, we want to find an approximation of the solution by solving it in a finite dimensional subspace. We discretize this problem using linear finite elements. First, we assume that the domain Ω has polygonal boundaries. Next, let $\mathcal{T}$ be a *triangulation* of Ω, with $\mathcal{N}$ denoting the set of its nodes. A set $\mathcal{T}$ of triangles T is a triangulation of Ω if

(i) $\overline{\Omega} = \bigcup_{T\in\mathcal{T}} T$,

(ii) The intersection of two triangles from $\mathcal{T}$ is either a common edge, a common node, or empty.

Define the finite element space

$$S := \{y \in C^0(\overline{\Omega}) \mid y \text{ is a linear polynomial on every } T \in \mathcal{T}\}, \tag{3.17}$$

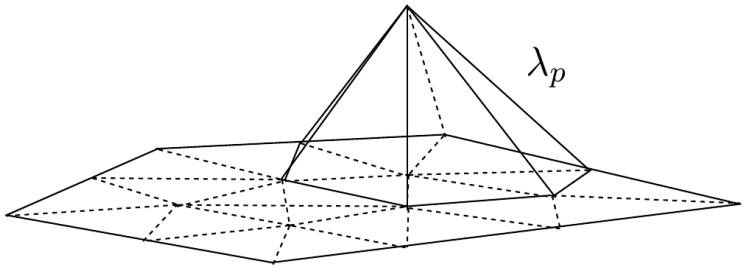

Figure 3.1: Basis function. Image adapted from [40].

It satisfies

$$S \times S \subset H^1(\Omega) \times L^2(\Omega). \tag{3.18}$$

To find solutions in $S \times S$, we need to choose a basis of this space. For $p \in \mathcal{N}$, let $\lambda_p \in S$ be a piecewise linear function satisfying

$$\lambda_p(q) = \delta_{pq} \qquad \forall q \in \mathcal{N} \qquad \textit{(Kronecker-}\delta\textit{)}. \tag{3.19}$$

Then,

$$\Lambda := \{\lambda_p \mid p \in \mathcal{N}\} \tag{3.20}$$

is a basis of S called nodal basis.

Thus, we can represent δV_k and δw_k as linear combinations of these first order basis functions:

$$\delta V_k = \sum_{p \in \mathcal{N}} a_p \lambda_p \qquad \text{and} \qquad \delta w_k = \sum_{q \in \mathcal{N}} a_q \lambda_q. \tag{3.21}$$

Plugging in this into (3.13) - (3.14), and choosing the basis functions as test func-

tions, we obtain the following system for the unknowns a_p, b_q, $\forall p, q \in \mathcal{N}$:

$$\begin{aligned}
\delta t_k \sum_{p\in\mathcal{N}} a_p \int_\Omega \nabla\lambda_p \cdot M\nabla\lambda_r dx + \delta t_k \sum_{p\in\mathcal{N}} a_p \int_{\partial\Omega} \alpha\lambda_p\lambda_r dx \\
+ \sum_{p\in\mathcal{N}} a_p \int_\Omega (1 - \delta t_k f_V(V_k, w_k))\lambda_p\lambda_r dx \\
-\delta t_k \sum_{q\in\mathcal{N}} b_q \int_\Omega f_w(V_k, w_k)\lambda_q\lambda_r dx = \delta t_k \int_{\partial\Omega} \beta\lambda_r dx \\
+\delta t_k \int_\Omega (\nabla \cdot M\nabla V_k + f(V_k, w_k))\lambda_r dx \\
\forall r \in \mathcal{N},
\end{aligned} \tag{3.22}$$

$$\begin{aligned}
-\delta t_k \sum_{p\in\mathcal{N}} a_p \int_\Omega g_V(V_k, w_k)\lambda_p\lambda_s dx + \sum_{q\in\mathcal{N}} b_q \int_\Omega (1 - \delta t_k g_w(V_k, w_k))\lambda_q\lambda_s dx \\
= \delta t_k \int_\Omega g(V_k, w_k)\lambda_s dx \qquad \forall s \in \mathcal{N}.
\end{aligned} \tag{3.23}$$

3.1.3 The linear system

The integrals in (3.22) - (3.23) contain no unknown functions, and are, therefore, constants that can be computed, for example, by a quadrature rule. Thus, we get a sparse linear system, with $2|\mathcal{N}|$ unknowns, where $|\mathcal{N}|$ is the cardinality of $\mathcal{N}$.

To solve the resulting linear system, the preconditioned biconjugate gradient stabilized method (Bi-CGSTAB) [48] is used - an iterative method that represents a variant of the Bi-Conjugate Gradients approach. The algorithm is presented in Alg. 1, where $K = K_1K_2 \approx A$ is used as preconditioner. In our implementation, the incomplete LU factorization [38] with fill level 1 is taken as preconditioner.

3.2 The Eikonal Model

The eikonal model does not depend on time. Therefore, only space discretization is needed, and, again, the solution is determined using the finite element method. How-

Algorithm 1 Preconditioned Bi-CGSTAB Algorithm [48]

let x_0 be an initial guess;
$r_0 = b - Ax_0$;
let $\overline{r}_0$ be an arbitrary vector, such that $(\overline{r}_0, r_0) \neq 0$, e.g. $\overline{r}_0 = r_0$;
$\rho_0 = \alpha = \omega_0 = 1$;
$v_0 = p_0 = 0$;
for $i = 1, 2, 3, ...$ **do**
  $\rho_i = (\overline{r}_0, r_{i-1})$;
  $\beta = (\rho_i/\rho_{i-1})(\alpha/\omega_{i-1})$;
  $p_i = r_{i-1} + \beta(p_{i-1} - \omega_{i-1}v_{i-1})$;
  determine y from $Ky = p_i$;
  $v_i = Ay$;
  $\alpha = \rho_i/(\overline{r}_0, v_i)$;
  $s = r_{i-1} - \alpha v_i$;
  determine z from $Kz = s$;
  $t = Az$;
  $\omega_i = (K_1^{-1}t, K_1^{-1}s)/(K_1^{-1}t, K_1^{-1}t)$;
  $x_i = x_{i-1} + \alpha y + \omega_i z$;
  if x_i is accurate enough **then**
    stop;
  end if
  $r_i = s - \omega_i t$;
end for

ever, since the resulting elliptic problem is nonlinear, a nonlinear solver is required. A damped Newton method has been chosen in this thesis.

Let us rewrite the eikonal model:

$$c_0\sqrt{\nabla u \cdot M\nabla u} - \nabla \cdot (M\nabla u) = \tau_m \qquad \text{on } \Omega, \tag{3.24}$$

$$\boldsymbol{n} \cdot M\nabla u + \alpha u = \beta \qquad \text{on } \partial\Omega. \tag{3.25}$$

As we are looking for a weak solution, we need to write equation (3.24) in its weak formulation:

$$c_0 \int_\Omega \sqrt{\nabla u \cdot M\nabla u}\phi dx + \int_\Omega \nabla u \cdot M\nabla\phi dx - \int_{\partial\Omega} \boldsymbol{n} \cdot M\nabla u\phi ds = \int_\Omega \tau_m \phi dx$$
$$\forall \phi \in H^1(\Omega). \tag{3.26}$$

Using (3.25) and rearranging, we get:

$$c_0 \int_\Omega \sqrt{\nabla u \cdot M\nabla u}\phi dx + \int_\Omega \nabla u \cdot M\nabla\phi dx + \int_{\partial\Omega} \alpha u\phi ds = \int_\Omega \tau_m \phi dx + \int_{\partial\Omega} \beta\phi ds$$
$$\forall \phi \in H^1(\Omega). \tag{3.27}$$

Additionally, $\partial\Omega$ can be divided into a Dirichlet boundary Γ_D and a Neumann boundary Γ_N:

$$\partial\Omega = \Gamma_D \cup \Gamma_N. \tag{3.28}$$

As before, since on the Neumann boundary we have a homogeneous condition, α and β must vanish there. On the Dirichlet boundary, however, we pick a very large α ($\approx 10^8$), and let $\beta := \alpha u_0$, to introduce a penalty for the Neumann part of equation (3.25). Here, u_0 represents the known value of the solution on the Dirichlet boundary. Using this and the fact that the boundary integrals in (3.27) can be

written as the sum of the integrals over the two subdomains, we obtain:

$$c_0 \int_\Omega \sqrt{\nabla u \cdot M \nabla u}\phi dx + \int_\Omega \nabla u \cdot M \nabla \phi dx + \int_{\Gamma_D} \alpha u \phi ds = \int_\Omega \tau_m \phi dx + \int_{\Gamma_D} \beta \phi ds$$
$$\forall \phi \in H^1(\Omega). \quad (3.29)$$

3.2.1 Space discretization

As for the monodomain model, we pick a conformal triangulation $\mathcal{T}^E$ of the spatial domain Ω, and let $\mathcal{N}^E$ be its set of nodes. Analogously to (3.17), we define the corresponding finite element space $S^E \subset H^1(\Omega)$, and basis functions λ_p^E as in (3.19). We can, therefore, decompose u as a linear combination of the basis functions:

$$u = \sum_{p \in \mathcal{N}^E} c_p \lambda_p^E. \quad (3.30)$$

Again, choosing the basis functions as test functions, equation (3.29) becomes:

$$c_0 \int_\Omega \sqrt{\nabla \left(\sum_{p \in \mathcal{N}^E} c_p \lambda_p^E \right) \cdot M \nabla \left(\sum_{p \in \mathcal{N}^E} c_p \lambda_p^E \right)} \lambda_q^E dx$$
$$+ \sum_{p \in \mathcal{N}^E} c_p \int_\Omega \nabla \lambda_p^E \cdot M \nabla \lambda_q^E dx + \sum_{p \in \mathcal{N}^E} c_p \int_{\Gamma_D} \alpha \lambda_p^E \lambda_q^E ds = \int_\Omega \tau_m \lambda_q^E dx + \int_{\Gamma_D} \beta \lambda_q^E ds$$
$$\forall q \in \mathcal{N}^E. \quad (3.31)$$

For the simulations in this thesis, second order basis functions have been used for the eikonal model.

3.2.2 The nonlinear system

Notice that due to the presence of the square root in the first integral on the left hand side, the system (3.31) is nonlinear. Therefore, a nonlinear solver is required.

Let us write the general form of such a system:

$$\text{find } y \text{ such that } F(y) = 0 \tag{3.32}$$

The common method of solving such systems is (a modification of) *Newton's method*. Here, an initially chosen initial guess of the solution is iteratively improved on. In the simplest variant of Newton's method, the iteration is

$$F_y(y_n)(y_{n+1} - y_n) = -F(y_n). \tag{3.33}$$

In the case when F is linear, the solution is obtained in one iteration step, independent of the initial guess. However, in the case when F is nonlinear – which is also our case – a number of iterations is required to reach the solution with the desired accuracy. Moreover, depending on the initial guess, the iteration might not converge. Therefore, a good initial guess is required. The more significant the nonlinearity is, the better the initial guess must be.

Since solving a linear system can be done immediately, in one step, one possible approach is to use *numerical continuation*. The idea is to first solve the linear part of problem to obtain an approximate solution. The linear problem in our case is

$$-\nabla \cdot (M\nabla u) = \tau_m. \tag{3.34}$$

Then, we gradually introduce the nonlinearity term, at each step using the previously obtained solution as initial value for the new problem. Specifically, for the eikonal model, we solve the equation

$$\gamma c_0 \sqrt{\nabla u \cdot M\nabla u} - \nabla \cdot (M\nabla u) = \tau_m, \tag{3.35}$$

for γ gradually increasing from 0 to 1. The parameter γ is called *continuation parameter*. If the solution of the Newton's method converges quickly for some value of γ, a larger increment is taken at the next step. If, on the other hand, it does not converge, the solution is reverted to the previous one and a smaller increase in the continuation parameter is used. When γ reaches 1, we will have obtained the solution of the original eikonal equation.

In this thesis, an error based damped Newton algorithm [7] (NLEQ-ERR) is used, as presented in Alg. 2. This method is specifically designed to solve nonlinear systems arising from the discretization of nonlinear PDEs. At each iteration step of Newton's method, linear systems of the form (3.33) need to be solved. As for the monodomain model, the Bi-CGSTAB solver is employed, with a zero level fill ILU preconditioner.

Algorithm 2 Error based damped Newton algorithm [7]

1: pick an error accuracy ϵ;
2: let x^0 be an initial guess; compute $F(x^0)$;
3: set a damping factor λ_0, with $\lambda_0 = 1$ or $\lambda_0 \ll 1$;
4: **for** $k = 0, 1, 2, ...$ **do**
5: evaluate Jacobian $F'(x^k)$; determine Δx_k from $F'(x^k)\Delta x_k = -F(x^k)$;
6: **if** $\|\Delta x^k\| < \epsilon$ **then**
7: $x^* = x^k + \Delta x^k$;
8: stop;
9: **end if**
10: **if** k > 0 **then**
11: $\mu_k = \dfrac{\|\Delta x^{k-1}\| \cdot \|\overline{\Delta x}^k\|}{\|\overline{\Delta x}^k - \Delta x^k\| \cdot \|\Delta x^k\|} \cdot \lambda_{k-1}$;
12: $\lambda_k = \min(1, \mu_k)$
13: **end if**
14: **if** $\lambda_k < \lambda_{min}$ **then**
15: stop; failure;
16: **end if**
17: $x^{k+1} = x^k + \lambda_k \Delta x^k$; evaluate $F(x^{k+1})$;
18: determine $\overline{\Delta x}^{k+1}$ from $F'(x^k)\overline{\Delta x}^{k+1} = -F(x^{k+1})$;
19: $\Theta_k = \dfrac{\|\overline{\Delta x}^{k+1}\|}{\|\Delta x^k\|}$;
20: $\mu'_k = \dfrac{0.5\|\Delta x^k\| \cdot \lambda_k^2}{\|\overline{\Delta x}^{k+1} - (1-\lambda_k)\Delta x^k\|}$;
21: **if** $\Theta_k \geq 1$ or , if restricted: $\Theta_k > 1 - \lambda_k/4$ **then**
22: replace λ_k by $\lambda'_k = \min(\mu'_k, 0.5\lambda_k)$;
23: **goto** line 14;
24: **else**
25: $\lambda'_k = \min(1, \mu'_k)$;
26: **end if**
27: **if** $\lambda_k = \lambda'_k = 1$ **then**
28: **if** $\|\overline{\Delta x}^{k+1} < \epsilon\|$ **then**
29: $x^* = x^k + \Delta x^k$;
30: stop;
31: **end if**
32: **else if** $\lambda'_k \geq 4\lambda_k$ **then**
33: replace λ_k by λ'_k;
34: **goto** line 17;
35: **end if**
36: **end for**

NOTE: All norms of corrections are understood as scaled smooth norms.

4 Model coupling

4.1 The need for coupling

The monodomain model provides accurate solutions describing the position and shape of the depolarization wavefront at each moment in time. An elliptic problem needs to be solved at each time step. A normal heartbeat lasts around one second. At the same time, the rapid kinetics have time constants ranging between 0.1 and 500 ms, which require time steps in some phases of 0.001 msec [16]. Thus, up to 10^6 time steps (and, therefore, solutions to elliptic problems) might be required to simulate an entire heartbeat.

Moreover, the depolarization wavefront is a very thin region, with the potential varying from its resting to the plateau value in a spatial region on the order of millimeters [43]. Thus, a discretization of the order of 0.1 mm is required in this region. Meaningful regions of the heart, however, are at a scale of several centimeters. So, in the case of a uniform grid in three dimensions, problems with $O(10^7)$ unknowns need to be solved at each time step. Parallel simulations and adaptive algorithms in both time and space have been designed to overcome these problems (see [16] and the references therein). In this thesis, however, we pursue another approach.

We notice that the eikonal model does not suffer from the shortcomings of the monodomain model mentioned in the previous paragraph. On the one hand, it does not depend on time, so no time integration is required. Barring the numerical continuation, only one elliptic problem needs to be solved. On the other hand, the spatial scales are much larger, since the solution describes the position in time of the wavefront, which varies over larger domains, and has, therefore, smaller gradients. The main disadvantages of the eikonal model are that it does not describe the shape of the excitation front, and, since it is derived from the monodomain model using

an approximation, it is less accurate. Additionally, in reality, due to the need of numerical continuation, not only one elliptic problem has to be solved, but several of them. However, since the number of continuation steps is in the order of $O(1)$, the additional computational time is insignificant. Thus, the idea is to use the monodomain model for the regions of the heart where a more accurate solution is required or the shape of the depolarization wavefront is needed, and the eikonal model in the rest of the computational domain.

Another circumstance when the eikonal model cannot be used alone is in the presence of a scar in the myocardium, where no reaction is taking place. As the eikonal model does not provide means of dealing with that, the monodomain model must be used in the region of the scar. Therefore, to determine the position of the wavefront throughout the entire myocardium, we use the eikonal model for the healthy area and the monodomain model around the scarred tissue, with a vanishing reaction term on the scar. The initiation region is, in this case, in the eikonal domain.

4.2 Coupling Conditions

Mathematically, we would like two conditions to be satisfied at the boundary of the different regions. The first one is the Dirichlet condition, i.e. the depolarization times should coincide for both areas. We need to have:

$$u_E(\boldsymbol{x}) = t \quad \text{where} \quad v_M(\boldsymbol{x}, t) = 0.5(v_r + v_p). \tag{4.1}$$

Here, u_E is the depolarization time in the eikonal domain, while v_M is the potential difference in the monodomain region.

Secondly, a Neumann condition needs to be satisfied, i.e. the flux through the common boundary should be equal:

$$\nabla u_M(\boldsymbol{x}) \cdot M\boldsymbol{n}(\boldsymbol{x}) = \nabla u_E(\boldsymbol{x}) \cdot M\boldsymbol{n}(\boldsymbol{x}), \tag{4.2}$$

where u_M is the depolarization time in the monodomain area and $\boldsymbol{n}$ is the unit normal to the boundary, while the integration is again over the boundary.

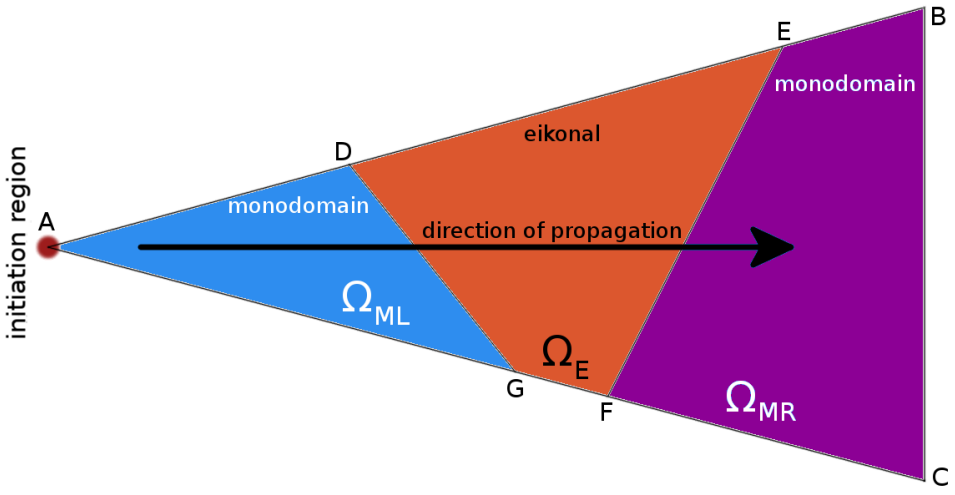

Figure 4.1: Example domain used to illustrate the coupling method.

If these two conditions were satisfied exactly, we would have perfect coupling. Numerically, however, this is an unattainable task.

4.3 Numerical implementation

We shall describe the numerical implementation of the coupling using an example of a domain decomposed into a region where the monodomain model is used, and a region where the eikonal model is implemented. The example can be seen in Fig. 4.1. The algorithm, however, can be applied to a general domain. The example domain Ω is divided into three regions:

- The left region Ω_{ML}, where the monodomain model is used,
- The middle region Ω_E, where the eikonal model is used,
- The right region Ω_{MR}, where again the monodomain model is used.

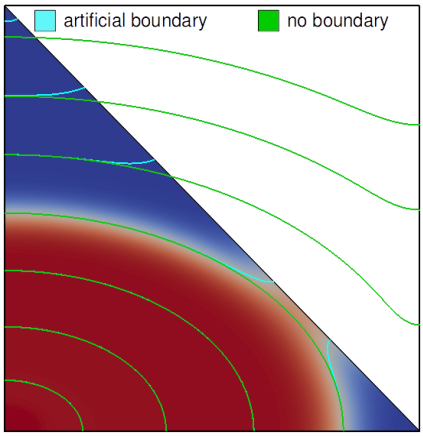

Figure 4.2: Wavefront curvature at an artificial boundary.

The excitation is initiated in a small region, in the left monodomain area. This initiation is implemented by setting a positive applied current in the neighborhood of point A

$$I_{app}(\boldsymbol{x}) > 0, \quad \forall \boldsymbol{x} \text{ with } |\boldsymbol{x} - A| < \delta, \tag{4.3}$$

and a vanishing applied current elsewhere. For boundaries AD, GA and DG of the left monodomain region, homogeneous Neumann conditions are set.

Since the initiation is around point A, the depolarization direction is from left to right. Consequently, the left monodomain simulation needs to be carried out first, then the eikonal one, and, finally, the right monodomain simulation.

In an unbounded domain, the depolarization wavefront is elliptic. When boundaries are present, however, due to the imposed Neumann conditions, the curvature of the wavefront changes close to the boundaries. Edges AB, AC, and BC represent physical boundaries, so the change in curvature is expected, and it is also present when simulating the entire domain using only one of the models. However, due to our division of the domain, there exists an additional boundary DG between the monodomain region Ω_{ML} and the eikonal region Ω_E (the new boundary EF will be discussed afterwards). This boundary is artificial, and changes in the curvature of the front are undesirable here. See Fig. 4.2 for a comparison of the isolines in a square domain and in a domain where an artificial boundary is introduced along a diagonal. To overcome this problem, the monodomain region is extended slightly,

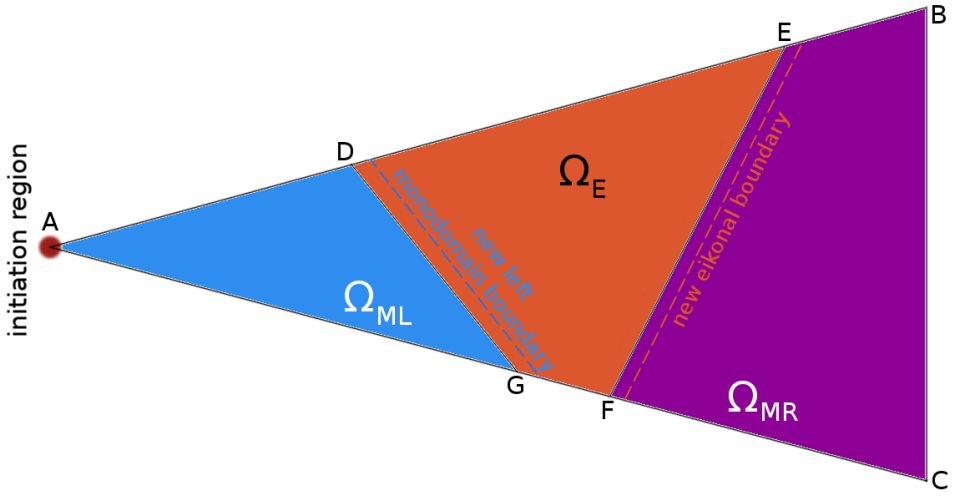

Figure 4.3: Example domain with extended regions.

so that the isolines of the solution still have an elliptic shape when they reach the eikonal boundary. The new boundary is imposed, parallel to the original one (see Fig. 4.3).

Next, DG is subdivided into smaller segments and the time step when the wavefront reaches the boundary (more specifically, when the potential at that point is at the middle value between the resting and plateau potentials) is stored for each division point. These values are then used for setting Dirichlet boundary conditions on the DG edge of the eikonal region Ω_E, i.e

$$u_E(\boldsymbol{x}) = \inf_{t>0}\{t \mid v_{ML}(\boldsymbol{x}, t) \geq 0.5(v_r + v_p)\}, \quad \forall \boldsymbol{x} \in DG. \tag{4.4}$$

Thus, the first coupling condition is enforced numerically. If the value of a point in between the subdivision points is needed, it is obtained by linearly interpolating the values of the neighboring points. If the discretization of the eikonal domain is known in advance, this algorithm can be improved by selecting the interpolation nodes of the eikonal boundary as subdivision points in the monodomain simulation. On the boundaries DE and FG, again homogeneous Neumann conditions are prescribed:

$$\boldsymbol{n} \cdot M \nabla u_E(\boldsymbol{x}) = 0, \quad \forall \boldsymbol{x} \in DE \cup FG. \tag{4.5}$$

The problem with the unrealistic wavefront curvature is also present at the boundary EF. Due to this reason, the eikonal region Ω_E is extended in the same way as in the previous case (again, see Fig. 4.3).

The simulation in the right monodomain region is initiated by setting Dirichlet boundary conditions on the EF edge, enforcing again the first coupling condition. Recall that, in the derivation of the eikonal equation, we assumed in (2.42) that the upstroke does not change significantly along the tissue, i.e.

$$v_{MR}(\boldsymbol{x}, t) = v_m(\omega),$$

for some function v_m that approximates the shape of the wavefront. Furthermore, in (2.53) we looked at the first order approximation of the function $T(\boldsymbol{\xi}, \omega)$

$$T(\boldsymbol{\xi}, \omega) := u_E(\boldsymbol{\xi}) + \frac{\omega}{s(\boldsymbol{\xi})}.$$

Solving for ω, we obtain:

$$\omega = (T(\boldsymbol{\xi}, \omega) - u_E(\boldsymbol{\xi}))\, s(\boldsymbol{\xi}). \tag{4.6}$$

Reverting to the original coordinates using (2.44), ω becomes

$$\omega = (t - u_E(\boldsymbol{x}))\, s(\boldsymbol{x}), \tag{4.7}$$

where t is the time in the right monodomain simulation, whereas $u_E(\boldsymbol{x})$ is the value at position $\boldsymbol{x}$ on the boundary, obtained from the eikonal simulation. Further, $s(\boldsymbol{x})$ can be determined from (2.63):

$$s(\boldsymbol{x}) = \frac{c_1}{\sqrt{\nabla u_E(\boldsymbol{x}) \cdot (M_m \nabla u_E(\boldsymbol{x}))}}. \tag{4.8}$$

Finally, an approximation v_m of the wavefront is needed. In this thesis, the function

$$v_m(\omega) = \frac{1}{2}\left(1 + \tanh\left(\tilde{c} \cdot \omega\right)\right), \tag{4.9}$$

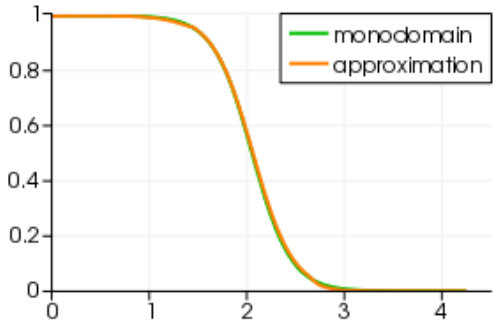

Figure 4.4: Comparison of the front approximation using (4.9) and the monodomain simulation result.

for some constant $\tilde{c}$ that determines the width of the front, and that can further be combined with c_1, is used. The comparison between the shape obtained using this approximation and the monodomain simulation result is shown in Fig. 4.4.

Putting everything together, Dirichlet values are set on EF according to

$$v_{MR}(\boldsymbol{x},t) = \frac{1}{2}\left(1+\tanh\left(c\cdot\frac{t-u_E(\boldsymbol{x})}{\sqrt{\nabla u_E(\boldsymbol{x})\cdot(M_m\nabla u_E(\boldsymbol{x}))}}\right)\right), \tag{4.10}$$

in the region undergoing depolarization (i.e. where $v_{MR}(\boldsymbol{x},t) > \epsilon$ and $v_{MR}(\boldsymbol{x},t) < 1-\epsilon$, for $\epsilon > 0$ small), where t is the current time in the right monodomain simulation, whereas $u_E(\boldsymbol{x})$, for all $\boldsymbol{x}$ on EF, represents the depolarization time according to the eikonal simulation in the Ω_E domain. On the boundary points where $v_{MR}(\boldsymbol{x},t) < \epsilon$ or $v_{MR}(\boldsymbol{x},t) > 1-\epsilon$, as well as on boundaries BC, CF and EB, a homogeneous Neumann condition is set. In summary, the algorithm is presented in Alg. 3.

The situation becomes more complex when there is more than one depolarization wavefront and the waves collide. In our example, this can be simulated by adding an initiation region in Ω_{MR}. In this case, the two different waves approach each other and then collide, a combined wave being created. Since the front coming from the right domain could influence the one from the left (or vice-versa), we can no longer do three sequential simulations: monodomain in the left area, then eikonal in the middle, and, finally, again monodomain in the right area. All regions must be simulated at each time step, and the values must be transfered in real time.

Algorithm 3 Model coupling

$v(\boldsymbol{x}, t_0) = 0$; $u_E(\boldsymbol{x}) = 0$;
$v(\boldsymbol{x}, t_0) = 1$ for $\boldsymbol{x}$ in the initiation region;
$k = 0$;
while not entire left monodomain region depolarized **do**
  set homogeneous Neumann BCs on all boundaries of the left monodomain region: $\nabla v_{ML}(\boldsymbol{x}, t_k) \cdot \boldsymbol{n} = 0$;
  execute one time step of the left monodomain simulation;
  $k = k + 1$;
  for all previously polarized points $\boldsymbol{x}$ on the left eikonal coupling boundary **do**
    if $v_{ML}(\boldsymbol{x}, t_k) \geq 0.5$ **and** $v_{ML}(\boldsymbol{x}, t_{k-1}) < 0.5$ **then**
      set Dirichlet BCs: $u_E(\boldsymbol{x}) = t_k$;
    end if
  end for
end while
on the other boundaries of the eikonal region set homogeneous Neumann BCs: $\nabla u_E(\boldsymbol{x}) \cdot \boldsymbol{n} = 0$;

execute eikonal simulation;

while not entire right monodomain region depolarized **do**
  for all points $\boldsymbol{x}$ on the monodomain coupling boundaries **do**
    $$v^k = \frac{1}{2}\left(1 + \tanh\left(c\frac{t_k - u_E(\boldsymbol{x})}{\sqrt{\nabla u_E(\boldsymbol{x}) \cdot (M_m \nabla u_E(\boldsymbol{x}))}}\right)\right);$$
    if $v^k > \epsilon$ **and** $v^k < 1 - \epsilon$ **then**
      set Dirichlet BCs: $v(\boldsymbol{x}, t_k) = v^k$;
    else
      set homogeneous Neumann BCs: $\nabla v_{MR}(\boldsymbol{x}, t_k) \cdot \boldsymbol{n} = 0$;
    end if
  end for
  elsewhere set homogeneous Neumann BCs: $\nabla v_{MR}(\boldsymbol{x}, t_k) \cdot \boldsymbol{n} = 0$;
  execute one time step of the monodomain simulations;
  $k = k + 1$;
end while

NOTE: If no subscript is indicated for v, it refers to both the left and right monodomain regions.

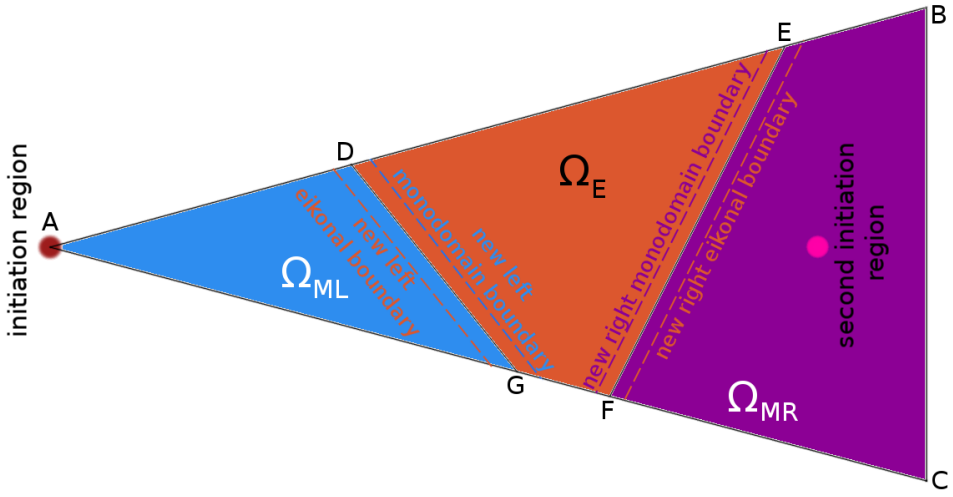

Figure 4.5: Example domain with extended regions in the more general case.

Additionally, the right monodomain region also needs to be extended, as in Fig. 4.5. The same holds for the left boundary of the eikonal domain. The new algorithm is shown in Alg. 4.

The same algorithm can be used without significant changes for more complex geometries or when a scar is present in the tissue. The difference is that, since the initiation of the excitation is in the eikonal domain in the case with a scar, the eikonal model needs to be simulated first. The initiation is then described by prescribing Dirichlet boundary conditions.

One remaining issue is how to determine the width of the domain extensions. This is where the second coupling condition is used. The width is chosen according to the relative error in the flux across the boundary:

$$\epsilon_{\text{flux}}^{\text{cond2}} = \frac{\int |\nabla u_M(\boldsymbol{x}) \cdot M\boldsymbol{n} - \nabla u_E(\boldsymbol{x}) \cdot M\boldsymbol{n}| d\boldsymbol{x}}{\int |\nabla u_M(\boldsymbol{x}) \cdot M\boldsymbol{n}| d\boldsymbol{x}}. \tag{4.11}$$

If the relative error is too high, the width of the extensions is increased.

Algorithm 4 General model coupling

$v(\boldsymbol{x}, t_0) = 0$; $u_E(\boldsymbol{x}) = 0$;
$v(\boldsymbol{x}, t_0) = 1$ for $\boldsymbol{x}$ in the initiation region;
execute one time step of the monodomain simulations;
$k = 1$;
while not entire domain depolarized **do**
  for all previously polarized points $\boldsymbol{x}$ on the eikonal coupling boundaries **do**
    if $v(\boldsymbol{x}, t_k) \geq 0.5$ **and** $v(\boldsymbol{x}, t_{k-1}) < 0.5$ **then**
      set Dirichlet BCs: $u_E(\boldsymbol{x}) = t_k$;
    else if $v(\boldsymbol{x}, t_k) < 0.5$ **then**
      set homogeneous Neumann BCs: $\nabla u_E(\boldsymbol{x}) \cdot \boldsymbol{n} = 0$;
    end if
  end for
  elsewhere set homogeneous Neumann BCs: $\nabla u_E(\boldsymbol{x}) \cdot \boldsymbol{n} = 0$;

  execute eikonal simulation;

  for all points $\boldsymbol{x}$ on the monodomain coupling boundaries **do**
    $v^k = \frac{1}{2}\left(1 + \tanh\left(c\frac{t_k - u_E(\boldsymbol{x})}{\sqrt{\nabla u_E(\boldsymbol{x}) \cdot (M_m \nabla u_E(\boldsymbol{x}))}}\right)\right)$;
    if $v^k > \epsilon$ **and** $v^k < 1 - \epsilon$ **then**
      set Dirichlet BCs: $v(\boldsymbol{x}, t_k) = v^k$;
    else
      set homogeneous Neumann BCs: $\nabla v(\boldsymbol{x}, t_k) \cdot \boldsymbol{n} = 0$;
    end if
  end for
  elsewhere set homogeneous Neumann BCs: $\nabla v(\boldsymbol{x}, t_k) \cdot \boldsymbol{n} = 0$;
  execute one time step of the monodomain simulations;
  $k = k + 1$;
end while

NOTE: If no subscript is indicated for v, it refers to both the left and right monodomain regions.

5 Numerical Results

Simulations on various two-dimensional geometries have been performed using the Kaskade 7 C++ Finite Element framework [17]. As parameters, the values shown in Table 5.1 have been used. These values are approximations corresponding to the canine myocardium [45]. Meshes have been generated either using the Kaskade 7 algoritms or using the Triangle software [41].

5.1 Independent simulations

First, let us compare the independent monodomain and eikonal simulations. Simulations have been executed on a rectangle of dimensions $16\,\mathrm{mm} \times 8\,\mathrm{mm}$. In the case of the eikonal model, the domain was divided into triangles with area of at most $0.5\,\mathrm{mm}^2$ and with a maximal interior angle of $30\,^\circ$. Thus, the mesh contains 244 nodes and 436 elements. For the monodomain simulation, a much finer resolution is needed, as the width of the wavefront is in the order of millimeters. The mesh in this case consists of triangles with area no greater than $0.0016\,\mathrm{mm}^2$, and the same angle condition as for the eikonal simulation. The resulting grid has 63776 nodes and 126771 triangles.

These numbers are considerably higher than those for the eikonal simulation. So, even simulating one time step of the monodomain model is expected to require more computational effort than solving the eikonal equation. This is certainly true if we make abstraction of the numerical continuation and Newton steps needed in the eikonal simulation. Nonetheless, as we shall see below, the number of continuation steps is almost always 2 for the chosen geometries, i.e. the equation needs to be solved once with no nonlinearity ($\gamma = 0$), and use the solution as initial condition for the equation with a full nonlinearity ($\gamma = 1$). Moreover, in simulations using

Parameter	Value	Parameter	Value
$M_{m_{11}}$	$0.64\,\mathrm{mm}^2$	I_{app}	10
$M_{m_{12}}$	$0\,\mathrm{mm}^2$	ϵ_1	0.01
$M_{m_{21}}$	$0\,\mathrm{mm}^2$	μ_1	0.07
$M_{m_{22}}$	$0.25\,\mathrm{mm}^2$	μ_2	0.3
τ_m	3 s	g_a	8.0
a	0.1	g_s	8.0
b	0.1	c_0	2.5

Table 5.1: Parameter values

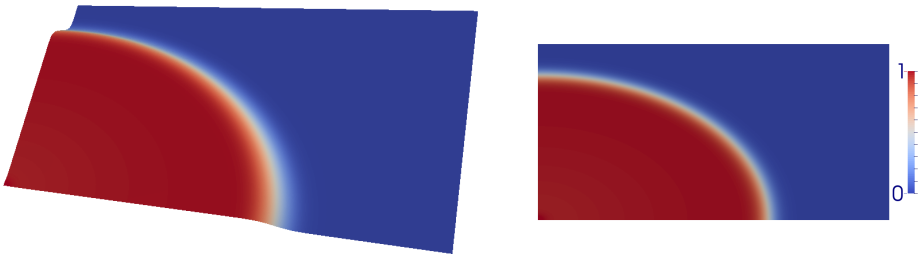

(a) Three-dimensional profile

(b) Two-dimensional projection

Figure 5.1: Monodomain simulation results at $t = 18\,\mathrm{ms}$.

Alg. 4, the fully nonlinear equation can be solved immediately (except at the first time step), by taking as initial guess the solution from the previous step, as the monodomain solution changes only slightly from one time step to another. This is also the reason why only a few Newton iterations are needed to obtain an eikonal solution with the desired accuracy.

Setting the initiation region in the bottom left corner of the domain, one would expect the front to travel towards the top right one. This is indeed the case, as can be seen in Fig. 5.1. This shows the potential in the myocardium at $t = 18\,\mathrm{ms}$. Red represents the depolarized region, whereas blue describes the region still polarized. Fig. 5.2 shows the time evolution of the wavefront at 6 ms intervals.

It is not possible to see this evolution using the eikonal model, as it only describes the time value when the wavefront reaches each point in space. Nonetheless, this means that the isoline with value t shows the position of the front at time t, i.e. all $\boldsymbol{x}$ satisfying $u(\boldsymbol{x}) = t$ are on the front at time t. Furthermore, these are all the points

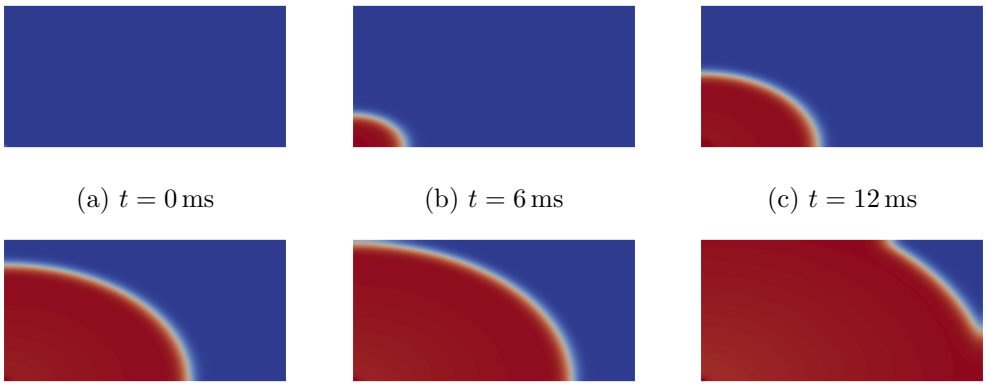

(a) $t = 0\,\text{ms}$ (b) $t = 6\,\text{ms}$ (c) $t = 12\,\text{ms}$

(d) $t = 18\,\text{ms}$ (e) $t = 24\,\text{ms}$ (f) $t = 30\,\text{ms}$

Figure 5.2: Monodomain simulation results.

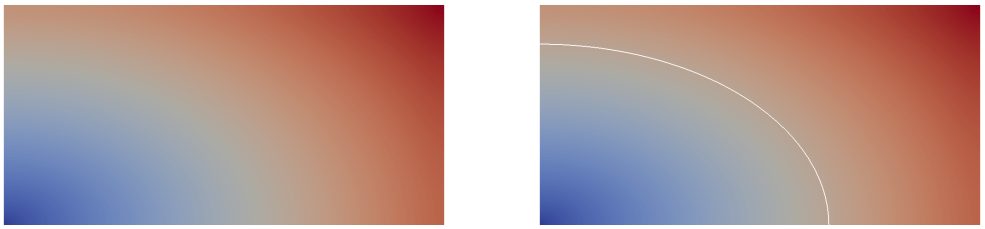

(a) Eikonal solution (b) Isoline at $t = 18\,\text{ms}$

Figure 5.3: Eikonal simulation results.

of the depolarization wavefront. The isoline corresponding to $t = 18\,\text{ms}$ is shown in Fig. 5.3.

In order to compare the results of the two individual models, the front position is shown at time intervals of 6 ms in Fig. 5.4. The isolines according to the monodomain model are shown in green, whereas the results of the eikonal model are drawn in white. The difference is barely noticeable. So, if only the position of the wavefront is required, the eikonal equations provide a good solution.

Finally, a (slightly) less accurate solution that does not describe the shape of the wavefront only makes sense if it significantly decreases the runtime of the algorithm. This is the case for the eikonal model, though. In our simulations, the monodomain

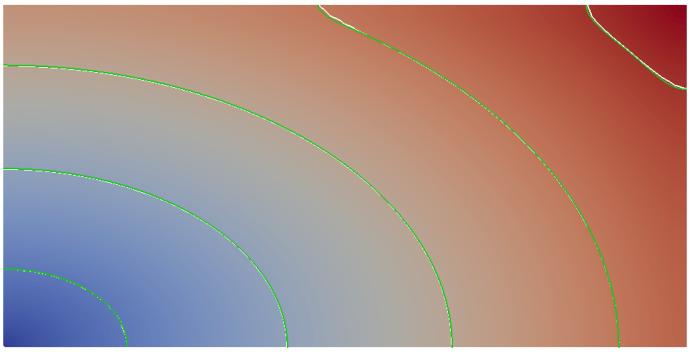

Figure 5.4: Wavefront position comparison for the monodomain and eikonal solutions at 6 ms intervals (monodomain - green, eikonal - white).

solution required 18805.13 s of computational time. The eikonal solution, on the other hand, needed only 0.13 s. This includes the time necessary for the numerical continuation, which in this case consisted of only two system solves: for $\gamma = 0$ and $\gamma = 1$.

5.2 Coupling with one excitation source

Now let us look at coupling results. The same rectangular domain we had for the individual simulations has now been divided into three parts, as in Fig. 5.5a. In two of them the monodomain model is used, whereas in the other one – the eikonal model. The initiation region is, as before, in the bottom left corner of the domain. The front will therefore first pass through the left monodomain region, then through the eikonal region, and, finally, through the right monodomain region. Note that this is a particular case of the geometry used to describe the coupling algorithm in section 4.3 (Fig. 4.1). Specifically, it was chosen since it is a case that one might expect could be problematic, due to the existence of a common point for the two monodomain regions.

The domains have been extended as seen in 5.5b. New boundaries have been set for the left monodomain and the eikonal regions at a distance of $0.5\sqrt{2}$ mm from

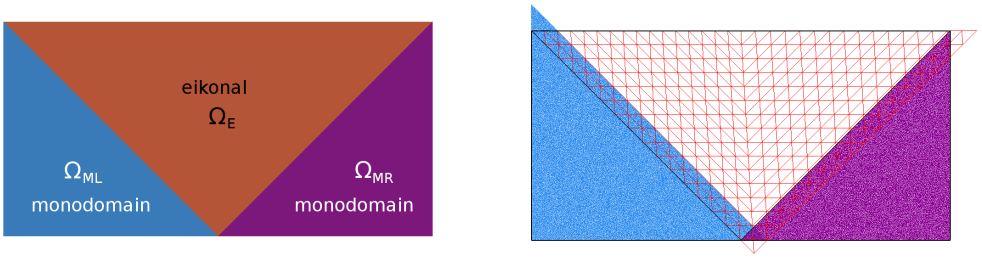

(a) Division of the domain

(b) Domain extensions

Figure 5.5: Coupling geometry.

the original ones. The original domain and its division is represented by the black lines. Moreover, not only the extensions are shown, but also the elements (triangles) composing the grid. One can notice that the density of elements is much higher for the monodomain regions than for the eikonal one.

The results of the coupling are presented in Fig. 5.6. The solution obtained using the monodomain model on the entire domain (i.e. the reference solution) is shown with green isolines, whereas the results obtained using model coupling are displayed with red isolines: dark orange in the monodomain region and light orange in the eikonal area.

One can see that the lines do not exactly overlap in the right monodomain region, especially near the common boundary of Ω_E and Ω_{MR} and at the top right corner. However, the reason of this inaccuracy stems from the results in the eikonal area, which are themselves not entirely precise. A closer inspection reveals that when approaching the right coupling boundary, the eikonal isolines slightly diverge from the full monodomain ones. This is explained by the same reasoning as that used in arguing the extensions of the domains. Specifically, due to the fact that an artificial boundary is introduced, with homogeneous Neumann boundary conditions, the isolines tend to become perpendicular to the artificial boundary, which does not happen in reality.

Quantitatively this can be shown by plotting the flux at the border between Ω_E and Ω_{MR}. The relative error in the flux on this boundary is $\epsilon_{\text{flux}}^{\text{cond2}} = 94.3\%$.

If the eikonal domain extension is doubled, a much more accurate solution is obtained

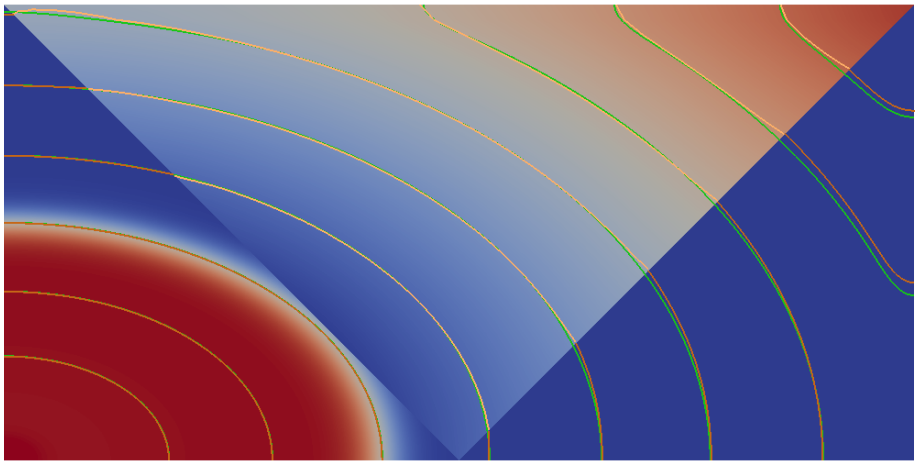

Figure 5.6: Wavefront position comparison for the full monodomain and model coupling solutions at 3 ms intervals (full monodomain - green, coupling - orange).

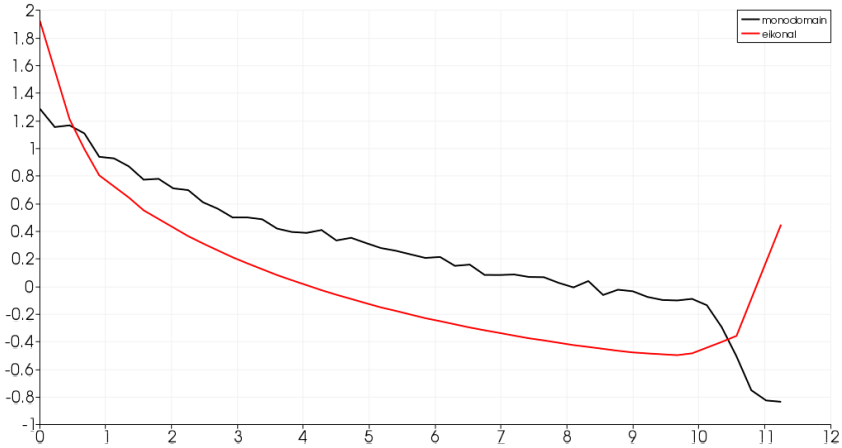

Figure 5.7: Flux at the right common boundary for the monodomain and eikonal regions.

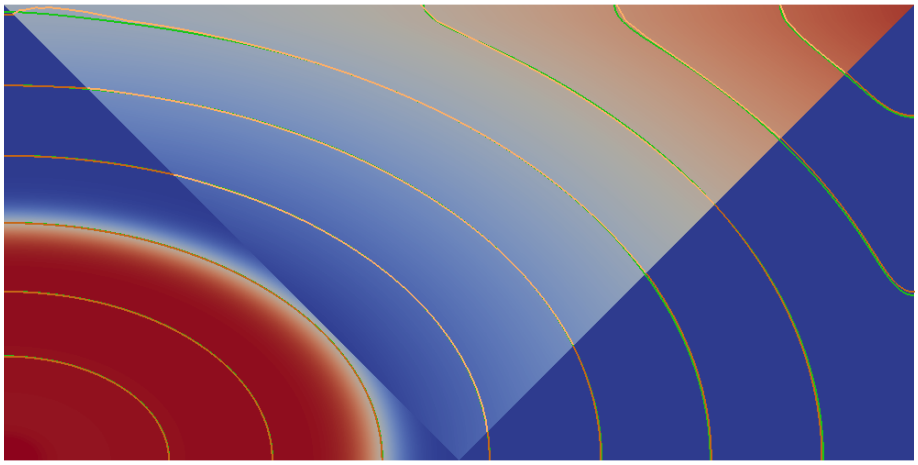

Figure 5.8: A more accurate solution of the coupling problem (full monodomain - green, coupling - orange).

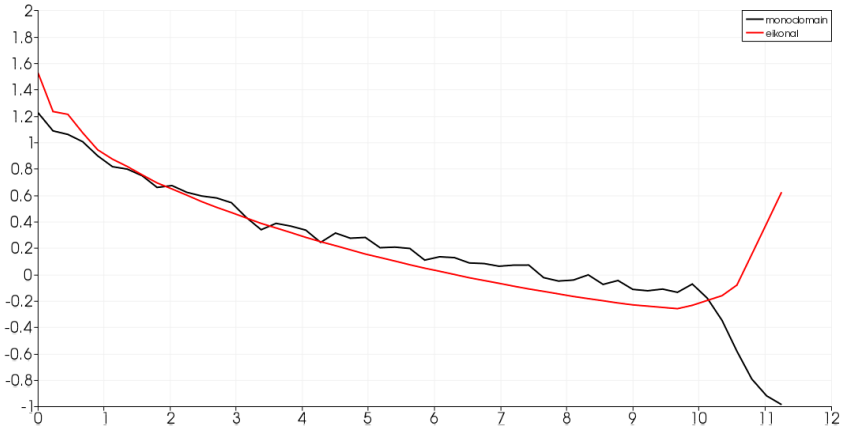

Figure 5.9: Flux at the right common boundary for the monodomain and eikonal regions for the more accurate solution.

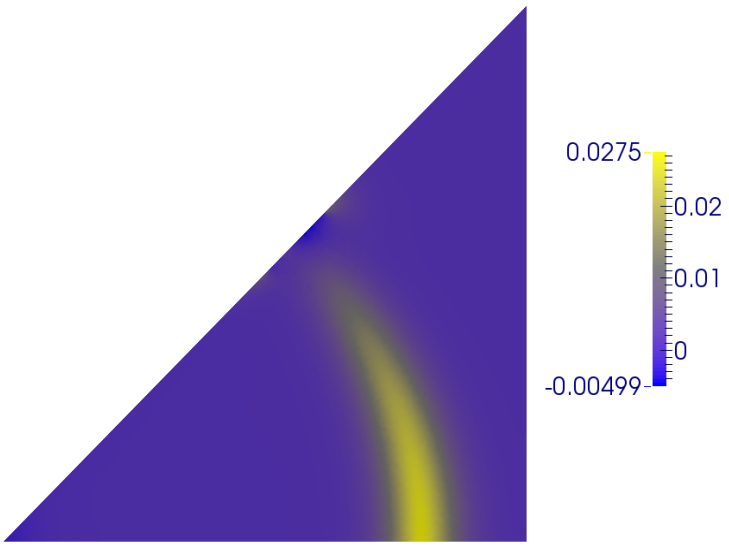

Figure 5.10: Difference between the full monodomain and coupling solutions on Ω_{MR} at $t = 24\,\text{ms}$.

(Fig. 5.8). The relative error in the flux is now much smaller at $\epsilon_{\text{flux}}^{\text{cond2}} = 41.5\%$. The difference between the full monodomain and the coupling solutions on the right monodomain region Ω_{MR} at $t = 24\,\text{ms}$ is shown in Fig. 5.10. Note the scaling of the picture. Whereas before the difference between the depolarized region (with value 1) and the polarized region (with value 0) was 1 nondimensional unit, now the difference between the maximum and minimum in the figure is 0.0324. Furthermore, the relative error in the L^2 norm has been computed for this part of the domain (at $t = 24\,\text{ms}$):

$$\epsilon_{\text{rel}} = \frac{\|V_{\text{FM}} - V_C\|_{L^2}}{\|V_{\text{FM}}\|_{L^2}} = 0.86\%, \tag{5.1}$$

where V_{FM} represents the full monodomain solution in this region, and V_C represents the solution obtained by the coupling of the models.

The runtime of this simulation was 6053.38 s, which is still significantly less than the full monodomain solution, that required 18805.13 s of computational time. Note that even though the number of nodes of the monodomain simulations has been reduced approximately by a half, the runtime decreased more than three times. This can be explained by the fact that the finite element solution is superlinear, and solving two

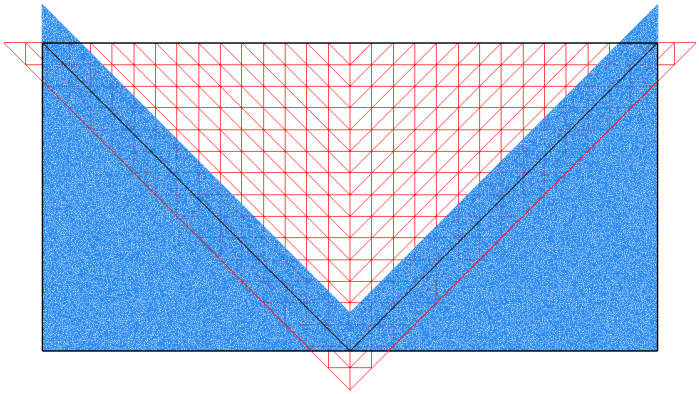

Figure 5.11: Domain extensions for the simulation with two sources.

independent problems requires less computational time than solving one problem with double the amount of nodes.

5.3 Coupling with two excitation sources

In a further simulation, the coupling algorithm was tested for situations where front collisions take place. The same domain and its decomposition as in Sec. 5.2 have been used. In this case, however, a new excitation source has been added in the bottom right corner of the domain. This second source is set to become active 3 ms after the first one. Thus, two wavefronts that collide, initially in the right monodomain region, and then in the eikonal area, are expected.

As mentioned in the end of Sec. 4.3, due to the existence of a second front in Ω_{MR}, this region also needs to be extended. The same holds for the left boundary of Ω_E. As the extended monodomain regions overlap, and, additionally, they both must be simulated at each time step, they have been combined into one single grid. This allows for a more accurate result and a simplified algorithm, but at a cost of a higher computational time, due to the superlinearity of the finite element solver. The extensions are shown in Fig. 5.11. As the two fronts influence each other, it is not sufficient to solve the eikonal equation only once, it needs to be solved at each

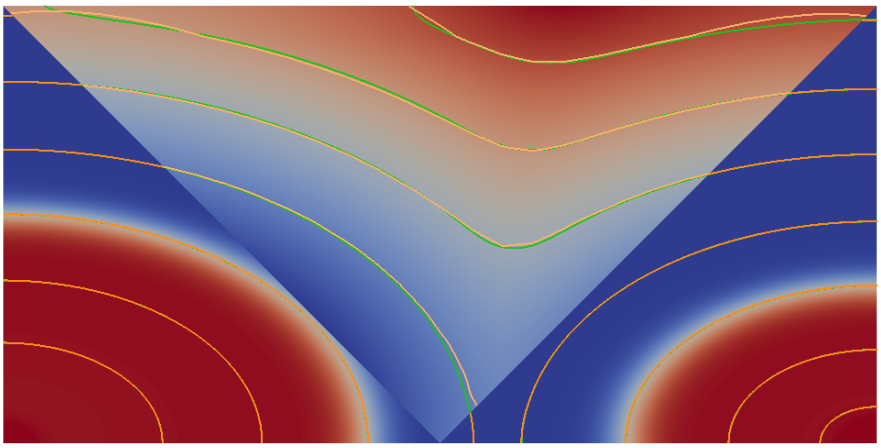

Figure 5.12: Wavefront position comparison for the full monodomain and model coupling solutions for two sources, with isolines at 3 ms intervals (full monodomain - green, coupling - orange).

time step. Thus, Alg. 4 is used.

The results are presented in Fig. 5.12. The isolines of the reference, full monodomain solution are again shown in green, whereas those corresponding to the model coupling - in orange (dark for the monodomain and light for the eikonal region). The relative flux error is $\epsilon_{\text{flux}}^{\text{cond2}} = 6.2\%$ for the left common boundary and $\epsilon_{\text{flux}}^{\text{cond2}} = 6.6\%$ for the right common boundary. The runtime of the solution was 11178.37 s. The increase, in contrast to the simulation with one initiation region, can be explained by the following reasons: the cumulative number of nodes for the monodomain simulation is higher due to the extension of the right monodomain region; the two monodomain regions have been combined into one; the eikonal problem needs to be solved at each time step; the overhead due to coupling is added at each time step, not only once as was the case before.

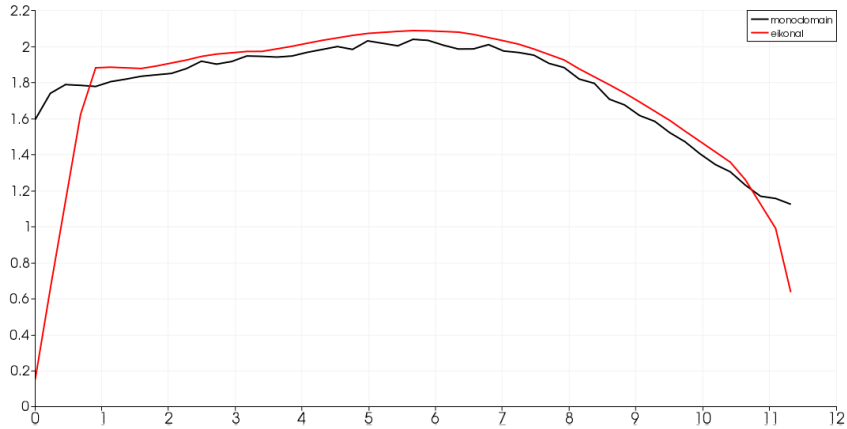

Figure 5.13: Coupling with two sources. Flux at the left common boundary for the eikonal and monodomain regions.

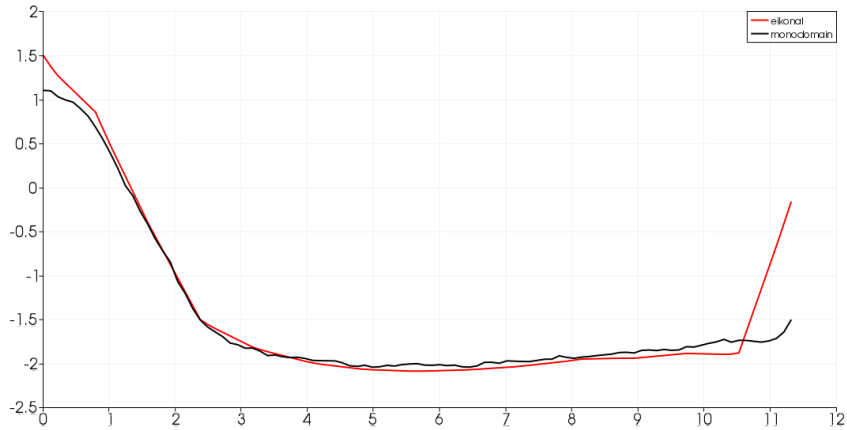

Figure 5.14: Coupling with two sources. Flux at the right common boundary for the eikonal and monodomain regions.

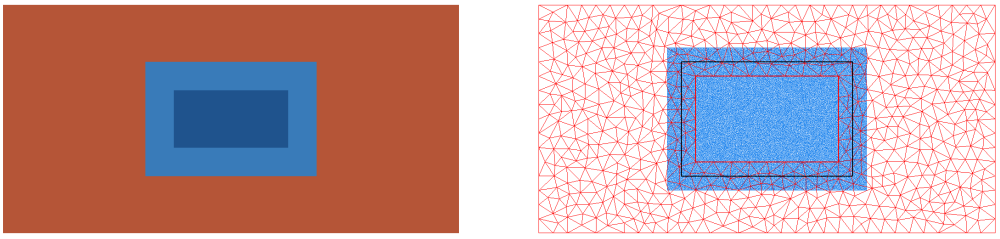

(a) Division of the domain (b) Domain extensions

Figure 5.15: Coupling geometry in the presence of scarred tissue.

5.4 Eikonal model with a scar

A case that the eikonal model does not account for is when a scar is present in the tissue. One could try to simply remove the scarred area from the computational domain. This would, however, imply that there is no conduction at all in the injured region, which is not true as there is conduction, but no reaction. On the other hand, this case is easy to be taken care of using the monodomain model, by removing the reaction term in the equations. Thus, model coupling would again provide a compromise. Specifically, this is done by using the eikonal model for the healthy tissue and the monodomain model for the scarred area and its immediate surroundings. Additionally, in contrast to using only the eikonal model, the coupling also allows us to see the position of the depolarization wavefront in the scarred area.

The geometry used for this simulation is shown in Fig. 5.15. As before, brown represents the eikonal region, whereas blue indicates the monodomain region. Additionally, dark blue shows the scarred tissue. Again, one excitation source is set in the bottom left corner of the grid.

The corresponding results can be seen in Fig. 5.16. The reference monodomain solution is in green and the coupling solution - in orange. In addition to that, the eikonal solution with the scarred area removed from the computational domain is shown in black. The model coupling provides an accurate solution with no noticeable differences to the full monodomain one. There is, however, a visible difference between these two and the eikonal solution in the region where the front has already

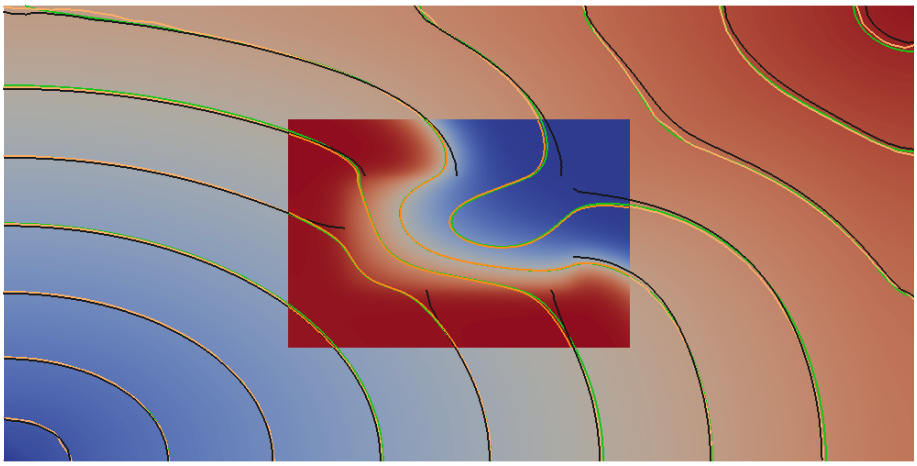

Figure 5.16: Wavefront position comparison for the full monodomain, model coupling and eikonal solutions in the presence of scarred tissue, with isolines at 3 ms intervals (full monodomain - green, coupling - orange, eikonal - black).

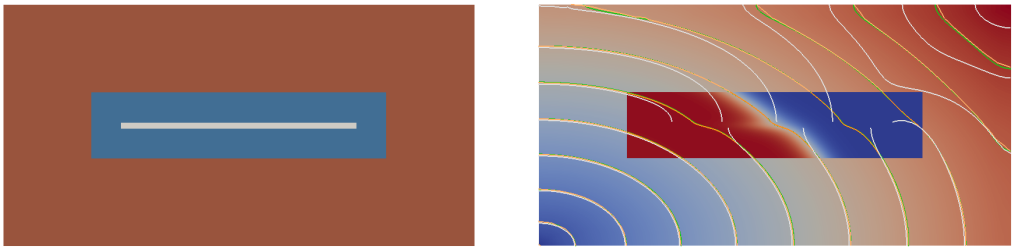

(a) Division of the domain

(b) Domain extensions

Figure 5.17: Coupling geometry in the presence of a very thin scarred tissue (full monodomain - green, coupling - orange, eikonal - white).

passed the scarred tissue and also near the boundaries of the scar. Again, the eikonal solution provides no results for the evolution of the depolarization wavefront in the scarred tissue.

The difference is even more apparent when the scar is very thin, as in Fig. 5.17a, where the scarred tissue is colored light gray. The results are shown in Fig. 5.17b, with white representing the eikonal only solution, whereas, as before, the reference monodomain solution is presented in green and the coupling solution - in orange. The isolines obtained using only the eikonal model significantly lag behind the coupling (and reference) solution. Although, due to the small area of the scar, its influence on the wavefront should be minimal, the eikonal solution fails to provide accurate results.

6 Conclusion

Two models for simulating the depolarization of cardiac cells have been presented. The first one – the monodomain model – is represented by a parabolic partial differential equation, coupled to ordinary differential equations that simulate the ionic current. The approach developed by Aliev and Panfilov has been used as a model for the ionic current, describing the excitation of cells as a propagating wavefront. This model is both time and space dependent. Also, due to the small width of the depolarization front, it requires a very fine spatial discretization.

The second – eikonal – model was derived from the first one, by making some additional assumptions, in particular, that the shape of the upstroke does not change significantly along the tissue. This allowed the elimination of the time variable, such that the new eikonal model is only space dependent. It is described by a nonlinear elliptic partial differential equation, that is much cheaper from a computational point of view, but also slightly less accurate. Moreover, in contrast to the monodomain model, it does not describe the shape of the wavefront, but only its position.

Numerical methods have been described for both models, the main ingredient being the Finite Element Method. These methods motivate the need for coupling the two models, i.e. using the monodomain model in the region where more accurate results or the shape of the wavefront are needed, and the eikonal model elsewhere. Conditions and algorithms for implementing this coupling for various situations have been shown.

Numerical results for various geometries have then been presented. First, the validity of the eikonal model has been demonstrated by comparing its results to the those generated using the monodomain model. Then, results for the coupling in a simple case with one excitation source have been presented. The collision of fronts was also of interest, so a new source has been added in a further simulation. Finally,

as the eikonal model does not make provisions for the case when a scar in present in the cardiac tissue, model coupling could be of use in this situation. Simulations have been performed for this case as well. In order to determine the accuracy of the coupling, all the results have been compared to reference solutions, obtained using the monodomain model in the entire domain.

An obvious direction for further work on this topic is extending the coupling to more irregular boundaries and to three spatial dimensions. In principle, the conditions and algorithms would be the same. Irregular domains might require different methods of solving the eikonal model, as argued in [45], so a Petrov-Galerkin method could be implemented. Additionally, one of the main issues in coupling the models is that artificial boundaries are introduced, that do not exist otherwise. The solution is significantly affected in the vicinity of these new boundaries. Instead of the approach used in this thesis of extending the domains, one could design transparent boundary conditions for the two models. Further, an existing method for decreasing the computational cost of the monodomain model is using mesh adaptivity [9, 16], which could be used in the monodomain regions of the model coupling as well.

Bibliography

[1] R. R. Aliev and A. V. Panfilov. "A simple two-variable model of cardiac excitation". In: *Chaos Solitons and Fractals* 7 (3 1996), pp. 293–301.

[2] O. Axelsson and V. A. Barker. *Finite Element Solution of Boundary Value Problems: Theory and Computation*. Academic Press, 1984.

[3] G. W. Beeler and H. Reuter. "Reconstruction of the action potential of ventricular myocardial fibres". In: *The Journal of Physiology* 268 (1 June 1977), pp. 177–210.

[4] Y. Bourgault, Y. Coudière, and C. Pierre. "Existence and uniqueness of the solution for the bidomain model used in cardiac electrophysiology". In: *Nonlinear Analysis: Real World Applications* 10 (1 2009), pp. 458–482.

[5] M. R. Boyett et al. "Modelling cardiac excitation and excitability". In: *Computational Biology of the Heart*. Ed. by A. V. Panfilov and A. V. Holden. John Wiley & Sons, 1997, pp. 1–47.

[6] P. Deuflhard, E. Hairer, and J. Zugck. "One-step and extrapolation methods for differential-algebraic systems". In: *Numerische Mathematik* 51 (5 1987), pp. 501–516.

[7] P. Deuflhard. *Newton Methods for Nonlinear Problems: Affine Invariance and Adaptive Algorithms*. Berlin Heidelberg: Springer Science & Business Media, 2004. Chap. 3.3, pp. 134–160.

[8] P. Deuflhard and F. Bornemann. *Numerische Mathematik 2*. German. Berlin, New York: de Gruyter Lehrbuch, 2008. Chap. 6.4.2, pp. 295–298.

[9] P. Deuflhard and M. Weiser. *Adaptive numerical solution of PDEs*. Berlin, Boston: De Gruyter, 2012.

[10] R. S. Eisenberg, V. Barcilon, and R. T. Mathias. "Electrical properties of spherical syncytia". In: *Biophysical Journal* 25 (1 1979), pp. 151–180.

[11] *Electrophysiological Studies*. Johns Hopkins Medicine. 2015. URL: http://www.hopkinsmedicine.org/healthlibrary/test_procedures/cardiovascular/electrophysiological_studies_92,p07971/ (visited on 02/05/2016).

[12] F. Fenton and A. Karma. "Vortex dynamics in three-dimensional continuous myocardium with fiber rotation: Filament instability and fibrillation". In: *Chaos: An Interdisciplinary Journal of Nonlinear Science* 8 (1 1998), pp. 20–47. DOI: http://dx.doi.org/10.1063/1.166311. URL: http://scitation.aip.org/content/aip/journal/chaos/8/1/10.1063/1.166311.

[13] R. A. FitzHugh. "Impulses and Physiological States in Theoretical Models of Nerve Membrane". In: *Biophysical Journal* 1 (6 1961), pp. 445–466.

[14] E. Flehmann et al. "Towards Patient Specific Catheter Selection: Computation of Aortic Geometry Based on Fused MRI Data". In: *Functional Imaging and Modeling of the Heart*. Ed. by D. N. Metaxas and L. Axel. New York: Springer, 2011, pp. 145–152.

[15] P. C. Franzone, L. Guerri, and S. Rovida. "Wavefront propagation in an activation model of the anisotropic cardiac tissue: asymptotic analysis and numerical simulations". In: *Journal of mathematical biology* 28 (2 1990), pp. 121–176.

[16] P. C. Franzone et al. "ADAPTIVITY IN SPACE AND TIME FOR REACTION-DIFFUSION SYSTEMS IN ELECTROCARDIOLOGY". In: *SIAM Journal on Scientific Computing* 28 (3 2006), pp. 942–962.

[17] S. Götschel, M. Weiser, and A. Schiela. "Solving Optimal Control Problems with the Kaskade 7 Finite Element Toolbox". In: *Advances in DUNE: Proceedings of the DUNE User Meeting, Held in October 6th-8th 2010 in Stuttgart, Germany*. Ed. by A. Dedner, B. Flemisch, and R. Klöfkorn. Berlin, Heidelberg: Springer Berlin Heidelberg, 2012, pp. 101–112. ISBN: 978-3-642-28589-9. DOI: 10.1007/978-3-642-28589-9_8. URL: http://dx.doi.org/10.1007/978-3-642-28589-9_8.

[18] J. L. Greenstein, R. Hinch, and R. L. Winslow. "Mechanisms of excitation-contraction coupling in an integrative model of the cardiac ventricular myocyte". In: *Biophysical journal* 90 (1 2006), pp. 77–91.

[19] J. L. Greenstein and R. L. Winslow. "An integrative model of the cardiac ventricular myocyte incorporating local control of Ca^{2+} release". In: *Biophysical journal* 83.6 (2002), pp. 2918–2945.

[20] C. S. Henriquez. "Simulating the electrical behaviour of cardiac tissue using the bidomain model". In: *Critical Reviews in Biomedical Engineering* 21 (1 1993), pp. 1–77.

[21] A. L. Hodgkin and A. F. Huxley. "A quantitative description of membrane current and its application to conduction and excitation in nerve". In: *The Journal of Physiology* 117 (4 1952), pp. 500–544.

[22] A. V. Panfilov and A. V. Holden, eds. *Modelling propagation in excitable Media*. John Wiley & Sons, 1997, pp. 65–99.

[23] W. T. M. III and D. B. Geselowitz. "Simulation Studies of the Electrocardiogram". In: *Circulation Research* 43 (2 1978), pp. 301–315.

[24] M. S. Jafri, J. J. Rice, and R. L. Winslow. "Cardiac Ca^{2+} dynamics: The roles of ryanodine receptor adaption and sarcoplasmic reticulum load". In: *Biophysical Journal* 74 (3 1998), pp. 1149–1168.

[25] J. P. Keener. "A Geometrical Theory for Spiral Waves in Excitable Media". In: *SIAM Journal on Applied Mathematics* 46 (6 1986), pp. 1039–1056. DOI: 10.1137/0146062. eprint: http://dx.doi.org/10.1137/0146062. URL: http://dx.doi.org/10.1137/0146062.

[26] B. Y. Kogan et al. "The simplified-FitzHugh-Nagumo model with action potential duration restitution: effects on 2D wave propagation". In: *Physica D* 50 (3 1991), pp. 327–340.

[27] W. Krassowska and J. C. Neu. "Effective boundary conditions for syncytial tissues". In: *IEEE Transactions on Biomedical Engineering* 41 (2 1994), pp. 143–150.

[28] K. Kunisch, C. Nagaiah, and M. Wagner. "A parallel Newton-Krylov method for optimal control of the monodomain model in cardiac electrophysiology". In: *Computing and Visualization in Science* 14 (6 2011), pp. 257–269.

[29] R. A. Luke et al. "Quantitative Analysis of Intercellular Connections by Immunohistochemistry of the Cardiac Gap Junction Protein Connexin43". In: *Circulation Research* 65 (5 1989), pp. 1450–1457.

[30] C. H. Luo and Y. Rudy. "A dynamic model of the cardiac ventricular action potential". In: *Circulation Research* 74 (6 1994), pp. 1071–1096.

[31] C. H. Luo and Y. Rudy. "A model of the ventricular cardiac action potential: Depolarisation, repolarisation, and their interaction". In: *Circulation Research* 68 (6 1991), pp. 1501–1526.

[32] R. E. McAllister, D. Noble, and R. W. Tsien. "Reconstruction of the electrical activity of cardiac Purkinje fibres". In: *The Journal of Physiology* 251 (1 1975), pp. 1–59.

[33] S. Mendis et al. *GLOBAL STATUS REPORT on noncommunicable diseases 2014*. Report. World Health Organization, 2014. (Visited on 05/12/2015).

[34] D. Noble. "A modification of the Hodgkin-Huxley equations applicable to Purkinje fibre action and pace-maker potentials". In: *Journal of Physiology* 160 (2 1962), pp. 317–352.

[35] D. Noble and R. L. Winslow. "Reconstructing the Heart: Network Models of SA Node-Atrial Interaction". In: *Computational Biology of the Heart*. Ed. by A. V. Panfilov and A. V. Holden. John Wiley & Sons, 1997, pp. 49–64.

[36] D. Noble et al. "Improved guinea-pig ventricular cell model incorporating a diadic space, IKr and IKs, and length- and tension-dependent processes". In: *Canadian Journal of Cardiology* 14 (1 1998), pp. 123–134.

[37] J. Roger and A. McCulloch. "A collocation-Galerkin finite element model of cardiac action potential propagation". In: *IEEE Transactions on Biomedical Engineering* 41 (8 1994), pp. 743–757.

[38] Y. Saad. *Iterative methods for sparse linear systems*. 2nd ed. SIAM, 2003. Chap. 10, pp. 301–321.

[39] F. B. Sachse. *Computational cardiology*. Berlin Heidelberg: Springer-Verlag, 2004. Chap. 6.1, pp. 120–56.

[40] F.-J. Sayas. *A gentle introduction to the Finite Element Method*. University of Delaware. 2008.

[41] J. R. Shewchuk. "Triangle: Engineering a 2D Quality Mesh Generator and Delaunay Triangulator". In: *Applied Computational Geometry: Towards Geometric Engineering*. Ed. by M. C. Lin and D. Manocha. Vol. 1148. Lecture Notes in Computer Science. From the First ACM Workshop on Applied Computational Geometry. Springer-Verlag, 1996, pp. 203–222.

[42] *Structure of the Heart. SEER Training Modules*. U. S. National Institutes of Health, National Cancer Institute. URL: http://training.seer.cancer.gov/anatomy/cardiovascular/heart/structure.html (visited on 01/26/2016).

[43] J. Sundnes et al. *Computing the Electrical Activity in the Heart*. Ed. by T. J. Barth et al. Springer, 2006. Chap. 1.

[44] M. Thiriet and K. H. Parker. "Physiology and pathology of the cardiovascular system: a physical perspective". In: *Cardiovascular Mathematics*. Ed. by L. Formaggia, A. Quarteroni, and A. Veneziani. MS&A. Milano: Springer-Verlag, 2009, pp. 1–46.

[45] K. A. Tomlinson. "Finite Element Solution of an Eikonal Equation for Excitation Wavefront Propagation in Ventricular Myocardium". Doctoral Thesis. The University of Auckland New Zealand, 2000.

[46] L. Tung. "A bi-domain model for describing ischemic myocardial D-C potentials". Doctoral Thesis. Cambridge, Mass., USA: Massachusetts Institute of Technology, 1978.

[47] *Underlying Cause of Death 1999-2013 on CDC WONDER Online Database*. Center for Disease Control and National Center for Health Statistics. 2015. URL: http://wonder.cdc.gov/ucd-icd10.html (visited on 05/12/2015).

[48] H. A. van der Vorst. "Bi-CGSTAB: A Fast and Smoothly Converging Variant of Bi-CG for the Solution of Nonsymmetric Linear Systems". In: *SIAM Journal on Scientific and Statistical Computing* 13 (2 1992), pp. 631–644.

[49] H. Wardhan and S. Singh. "Modeling of generation and propagation of cardiac action potential using fractional capacitance". In: *IOSR Journal of Biotechnology and Biochemistry* 1 (2 2015), pp. 1–11.

[50] N. Wiener and N. Rosenbluth. "The mathematical formulation of the problem of conduction of impulses in a network of connected excitable elements, specifically in cardiac muscle". In: *Archivos del Instituto de Cardiologia de Mexico* 16 (3 1946), pp. 205–265.

[51] R. L. Winslow et al. "Mechanisms of altered excitation-contraction coupling in canine tachycardia-induced heart failure, II, model studies". In: *Circulation Research* 84 (1999), pp. 571–586.

[52] D. W. Zhu et al. "The Value of Electrophysiology Study and Prophylactic Implantation of Cardioverter Defibrillator in Patients with Hypertrophic Cardiomyopathy". In: *Pacing and Clinical Electrophysiology* 21 (1 1998).